

Chimney-like intense pelagic upwelling in the center of basin-scale cyclonic gyres in large Lake Geneva

Seyed Mahmood Hamze-Ziabari¹, Ulrich Lemmin², Mehrshad Foroughan³, Rafael S. Reiss³, and D. Andrew Barry³

¹Ecole Polytechnique Fédérale de Lausanne

²Ecole Polytechnique Federale de Lausanne

³École Polytechnique Fédérale de Lausanne

December 21, 2022

Abstract

Basin-scale quasi-geostrophic gyres are common features of large lakes subject to Coriolis force. Cyclonic gyres are often characterized by dome-shaped thermoclines that form due to pelagic upwelling which takes place in their center. At present, dynamics of pelagic upwelling in the Surface Mixed Layer (SML) of oceans and lakes are poorly documented. A unique combination of high-resolution 3D numerical modeling, satellite imagery and field observations allowed confirming for the first time in a lake, the existence of intense pelagic upwelling in the center of cyclonic gyres under strong shallow (summer) and weak deep (winter) stratified conditions/thermocline. Field observations in Lake Geneva revealed that surprisingly intense upwelling from the thermocline to the SML and even to the lake surface occurred as chimney-like structures of cold water within the SML, as confirmed by Advanced Very High-Resolution Radiometer data. Results of a calibrated 3D numerical model suggest that the classical Ekman pumping mechanism cannot explain such pelagic upwelling. Analysis of the contribution of various terms in the vertically-averaged momentum equation showed that the nonlinear (advective) term dominates, resulting in heterogeneous divergent flows within cyclonic gyres. The combination of nonlinear heterogeneous divergent flow and 3D ageostrophic strain caused by gyre distortion is responsible for the chimney-like upwelling in the SML. The potential impact of such pelagic upwelling on long-term observations at a measurement station in the center of Lake Geneva suggests that caution should be exercised when relying on limited (in space and/or time) profile measurements for monitoring and quantifying processes in large lakes.

Hosted file

952398_0_art_file_10547762_rn5gbf.docx available at <https://authorea.com/users/568330/articles/614216-chimney-like-intense-pelagic-upwelling-in-the-center-of-basin-scale-cyclonic-gyres-in-large-lake-geneva>

Hosted file

952398_0_supp_10546995_rn56b6.docx available at <https://authorea.com/users/568330/articles/614216-chimney-like-intense-pelagic-upwelling-in-the-center-of-basin-scale-cyclonic-gyres-in-large-lake-geneva>

1 **Chimney-like intense pelagic upwelling in the center of basin-scale cyclonic gyres in**
2 **large Lake Geneva**

3 **S. M. Hamze-Ziabari, U. Lemmin, M. Foroughan, R. S. Reiss, D. A. Barry**

4
5
6
7 Ecological Engineering Laboratory (ECOL), Institute of Environmental Engineering (IIE),
8 Faculty of Architecture, Civil and Environmental Engineering (ENAC), Ecole Polytechnique
9 Fédérale de Lausanne (EPFL), 1015 Lausanne, Switzerland

10 Corresponding author: Seyed Mahmood Hamze-Ziabari (mahmood.ziabari@epfl.ch)

11 **Key Points:**

- 12 • Pelagic upwelling in the center of cyclonic gyres studied by 3D numerical modeling is
13 confirmed by field measurements and remote sensing imagery.
- 14 • Chimney-like pelagic upwelling that reached the surface was induced by cyclonic gyres
15 in the surface mixed layer during summer and winter.
- 16 • The 3D ageostrophic strain field caused by gyre distortion, not Ekman pumping,
17 produced a dome-shaped thermocline and upwelling in the pelagic zone.

18 Abstract

19 Basin-scale quasi-geostrophic gyres are common features of large lakes subject to Coriolis force.
20 Cyclonic gyres are often characterized by dome-shaped thermoclines that form due to pelagic
21 upwelling which takes place in their center. At present, dynamics of pelagic upwelling in the
22 Surface Mixed Layer (SML) of oceans and lakes are poorly documented. A unique combination
23 of high-resolution 3D numerical modeling, satellite imagery and field observations allowed
24 confirming for the first time in a lake, the existence of intense pelagic upwelling in the center of
25 cyclonic gyres under strong shallow (summer) and weak deep (winter) stratified
26 conditions/thermocline. Field observations in Lake Geneva revealed that surprisingly intense
27 upwelling from the thermocline to the SML and even to the lake surface occurred as chimney-
28 like structures of cold water within the SML, as confirmed by Advanced Very High-Resolution
29 Radiometer data. Results of a calibrated 3D numerical model suggest that the classical Ekman
30 pumping mechanism cannot explain such pelagic upwelling. Analysis of the contribution of
31 various terms in the vertically-averaged momentum equation showed that the nonlinear
32 (advective) term dominates, resulting in heterogeneous divergent flows within cyclonic gyres.
33 The combination of nonlinear heterogeneous divergent flow and 3D ageostrophic strain caused
34 by gyre distortion is responsible for the chimney-like upwelling in the SML. The potential
35 impact of such pelagic upwelling on long-term observations at a measurement station in the
36 center of Lake Geneva suggests that caution should be exercised when relying on limited (in
37 space and/or time) profile measurements for monitoring and quantifying processes in large lakes.

38 Plain Language Summary

39 Understanding the dynamics of Pelagic Upwelling (PU) is important because it can rapidly
40 transport nutrients upwards from the thermocline into the phototrophic zone and thus can affect
41 the bio-geo-chemical balance of the lake. Pelagic upwelling occurs in the center of cyclonic
42 gyres which have been observed in large lakes subject to Coriolis force. At present, little is
43 known about PU, because the processes associated with PU cannot be captured by the low-
44 resolution numerical models typically used to investigate geostrophic processes, and high-
45 resolution field observations are lacking. Therefore, in this study, high-resolution field
46 measurements were combined with 3D numerical simulations and satellite imagery to investigate
47 the PU structure in the center of a cyclonic gyre in Lake Geneva under different stratification
48 conditions. Field observations documented for the first time in a lake, details of the 3D velocity

49 and temperature fields in cyclonic gyres. They showed that PU forms a chimney-like structure of
50 cold water in the center of a cyclonic gyre. The chimney originates in the thermocline layer and
51 can reach the lake surface, as confirmed by satellite images. As the thermocline descends during
52 the cooling season, the chimney-like upwelling can attain a height of 80 m in winter.

53 **1 Introduction**

54 In most thermally stratified large lakes subject to Coriolis force, differential wind action
55 across the surface causes basin-scale gyres to form (Akitomo et al., 2009; Csanady, 1973;
56 Lemmin & D'Adamo, 1996; Shimizu et al., 2007). Gyres are large-scale coherent circulations
57 that play a critical role in the vertical and horizontal transport of nutrients, dissolved inorganic
58 carbon, heat, sediment and algae in large lakes (Ishikawa et al., 2002; Ji & Jin, 2006). The
59 interplay of vertical density stratification, Coriolis force, and irregularity in basin shape affects
60 the formation of gyres (Mortimer, 2004; Valerio et al., 2017). Depending on the sign of the
61 rotation, gyres can be characterized either by positive vorticity and a high-pressure core
62 (cyclonic gyre) or negative vorticity and a low-pressure core (anticyclonic gyre). Basin-scale
63 counterclockwise rotating (cyclonic) gyres are ubiquitous in most large Northern Hemisphere
64 lakes (e.g., Beletsky & Schwab, 2008; Csanady, 1973; Laval et al., 2005); however, clockwise
65 rotating (anticyclonic) gyres can also be formed due to Ekman pumping driven by anticyclonic
66 vorticity in surface winds (e.g., Beletsky et al., 2013). In the present study, we will focus on
67 cyclonic gyres, in particular on pelagic upwelling in their center, and investigate the dynamics
68 during different seasons in Lake Geneva.

69 In most thermally stratified lakes, a basin-scale cyclonic circulation is accompanied by a
70 dome-shaped thermocline having a shallower depth in the center of the lake than at the nearshore
71 (Csanady, 1968, 1977). On the other hand, a bowl-shaped thermocline (i.e., deeper in the center
72 of the lake and shallower in the nearshore) can be formed within an anticyclonic gyre (Beletsky
73 et al., 2012). Resulting physical processes such as upwelling and downwelling in the coastal and
74 pelagic areas of lakes can significantly affect the functioning of the lake ecosystem (Corman et
75 al., 2010; Ostrovsky & Sukenik, 2008) by changing the physical (e.g., temperature, currents) and
76 chemical (e.g., pollution, salinity) conditions of the water column, and consequently, biological
77 processes such as phytoplankton growth and bacterial life cycles (Lovecchio et al., 2022;
78 Troitskaya et al., 2015). The vertical motions associated with gyre dynamics can locally transport

79 nutrients from the metalimnion and hypolimnion into the epilimnion layer, potentially creating
80 hot spots of biological activity (Corman et al., 2010; Romanovsky & Shabunin, 2002; Troitskaya
81 et al., 2015).

82 Previous studies suggested two physical mechanisms to explain the formation of pelagic
83 upwelling at the center of a cyclonic circulation during summertime: (i) differential heating
84 (baroclinic effect) and (ii) Ekman transport caused by cyclonic surface winds. Using a simple
85 conceptual model, Csanady (1977) analyzed the combined effect of wind stress drift and
86 differential heating in nearshore-offshore regions, where shallow nearshore regions warm faster
87 than deeper mid-lake regions. For Lake Ontario, this combination produced a dome-shaped
88 thermocline during summer. Baroclinic effects due to a dome-shaped thermocline can generate a
89 pressure gradient between the mid-lake and nearshore regions, which can lead to/contribute to
90 the formation of cyclonic circulations (Beletsky et al., 2013). However, a numerical study by
91 Schwab et al. (1995) showed that imposing a zero-heat flux condition at a sloping lake boundary
92 can also form a dome-shaped thermocline.

93 Furthermore, a dome-shaped thermocline can be generated by the divergence of Ekman
94 transport, i.e., Ekman pumping, caused by cyclonic wind stress curl (Gill, 1982). Although
95 observational evidence for Ekman pumping is rare in physical limnology, wind stress curl, on the
96 other hand, has been reported over many large lakes (e.g., Lake Superior (Bennington et al.,
97 2010); Lake Michigan (Schwab & Beletsky, 2003); Lake Biwa (Japan; Endoh et al., 1995); Lake
98 Tahoe (USA; Strub & Powell, 1986); Lake Geneva (Lemmin & D'Adamo, 1996), suggesting
99 that such a mechanism may contribute to the formation of dome- or bowl-shaped thermoclines.
100 In the pelagic region, cyclonic/ anticyclonic wind fields cause, respectively, near-surface
101 divergence/convergence and surface-level depression/elevation, which in turn creates a dome-
102 shaped/bowl-shaped thermocline induced by upwelling/downwelling in the mid-lake region. The
103 “deformed” thermocline and the water surface level change produced by such a process can
104 result in horizontal pressure gradients, which can contribute to the formation of pelagic cyclonic
105 or anticyclonic circulations.

106 Nearshore upwelling has been investigated in various lakes (e.g., Corman et al., 2010;
107 Flood et al., 2020; Plattner et al., 2006; Pöschke et al., 2015; Reiss et al., 2020; Rowe et al.,
108 2019; Valbuena et al., 2022). However, few studies have reported on dome- or bowl-shaped

109 thermoclines in lakes and pelagic upwelling/downwelling during summer (e.g., Beletsky et al.,
110 2012). Field observations conducted in Lake Issyk-Kul (Kirgistan) showed that an increase of
111 dissolved oxygen in the surface layer occurs in the pelagic upwelling zone (Romanovsky &
112 Shabunin, 2002). In Lake Tanganyika (Africa), Corman et al. (2010) found that pelagic
113 upwelling can strongly affect the temporal pattern of temperature, nutrients, and phytoplankton
114 chlorophyll. More recently, Troitskaya et al. (2015) used in situ and remote sensing data to
115 identify pelagic upwelling in Lake Baikal (Russia) during summer.

116 The sparse previous pelagic upwelling field observations in lakes were typically limited
117 to at most a few moorings. Thus, they cannot provide a direct, detailed description of large-scale
118 gyre patterns and the associated pelagic upwelling (Beletsky et al., 2013; Hui et al., 2021).
119 Although upwelling and downwelling in the center of basin-scale gyres are well known from
120 theory, there are no reports of the transport of thermocline water to the epilimnion layer or even
121 to the lake surface caused by pelagic upwelling. This is likely due to (i) the difficulty of taking
122 detailed, high-resolution field observations of temperature profiles and velocity fields that can
123 confirm the existence of such patterns, and (ii) the fact that pelagic upwelling cannot be captured
124 by the low-resolution numerical models often used to investigate geostrophic processes in large
125 lakes (Brannigan, 2016). Lu et al. (2020) demonstrated in theory that a Tropical Cyclone (TC)
126 can cause vertical perturbations in the Surface Mixed Layer (SML) of cyclonic and anticyclonic
127 eddies, and a chimney-like upwelling, i.e., a cylinder of well-mixed cold water, can appear in the
128 Ekman layer. However, a cyclonic wind stress of TC intensity is rare over most lakes.

129 Previous studies have shown that pelagic upwelling in gyres and eddies exists in lakes.
130 Infrared and optical sensors such as the Advanced Very High-Resolution Radiometer (AVHRR)
131 are often applied to distinguish the signatures of coastal and pelagic upwelling in lakes and
132 oceans (Gutiérrez et al., 2011; Pisoni et al., 2014). However, detailed field measurement
133 identification of its structure are lacking. In particular, vertical dynamics associated with
134 cyclonic gyres in the absence of cyclonic wind stress has not been studied in lakes. Therefore, in
135 order to help fill this knowledge gap, we will investigate the formation mechanism of a chimney-
136 like pelagic upwelling in the SML of Lake Geneva in the absence of wind during the
137 development and propagation of gyres. Lake Geneva exhibits frequent and predictable cyclonic
138 and anticyclonic gyres after strong wind events (Hamze-Ziabari et al., 2022a), thus making it an
139 ideal site to study vertical transport associated with gyres. To carry out this investigation,

140 spatially detailed in situ measurements of temperature and velocity profiles accompanied by
141 high-resolution three-dimensional (3D) numerical modeling and remote sensing (AVHRR)
142 imagery were employed to capture the cyclonic circulation and associated intense upwelling
143 during both the strongly and weakly stratified seasons. The following questions will be
144 addressed:

- 145 • Can field measurements confirm the detailed temperature and current structure of a
146 cyclonic gyre in the center of the lake that was predicted by high-resolution 3D
147 modeling?
- 148 • How stable are the gyre and the pelagic upwelling in time and space? How can this be
149 verified?
- 150 • What effect does the seasonal change in stratification have on the development of the
151 gyre and the pelagic upwelling?
- 152 • Is the dome-shaped thermocline and the pelagic upwelling caused by Ekman pumping? If
153 not, what alternative processes can explain them?
- 154 • What is the potential impact of such upwelling on vertical profile data collected at a
155 longterm monitoring station located in the area where the strongest pelagic upwelling is
156 detected?

157 The Supplementary Information (SI) section provides complementary texts and figures
158 identified with prefix S.

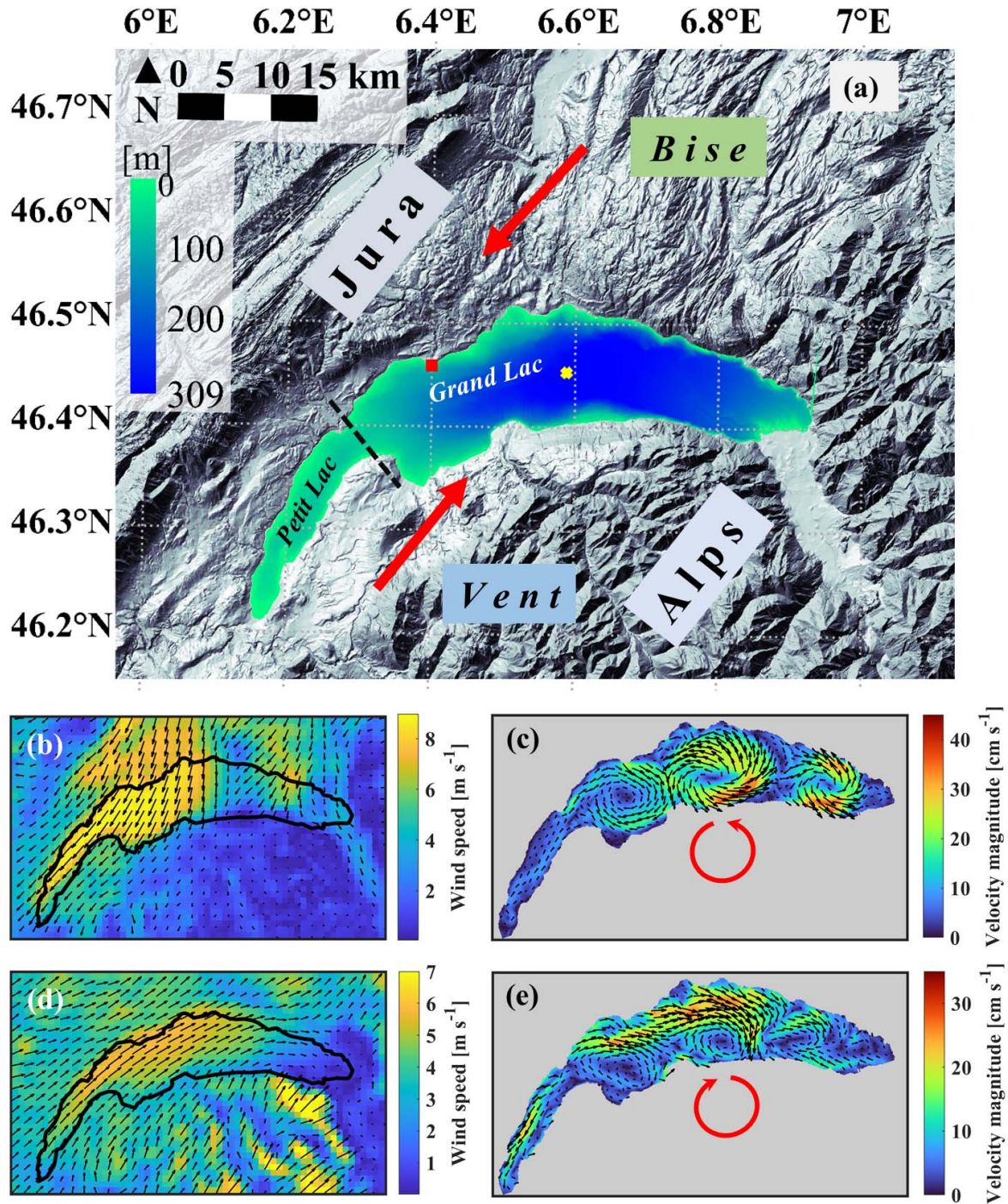
159 **2 Materials and Methods**

160 2.1 Field Site

161 Lake Geneva (local name: *Lac Léman*), the largest lake in Western Europe, is located
162 between Switzerland and France (Figure 1a). It is composed of two basins: the large *Grand Lac*
163 in the east (maximum depth 309 m), and the small, narrow *Petit Lac* in the west (maximum
164 depth ~ 70 m). The lake has a surface area of 580 km², a volume of 89 km³, and a length of ~70
165 km along its main arc. Its maximum width is 14 km. The lake is surrounded by the Alps to the
166 south and east, and the Jura mountains to the northwest. Due to the mountainous topography of
167 the surrounding area, there are two strong dominant wind fields, the *Bise* coming from the

168 northeast and the *Vent*, from the southwest. The central and western parts of the lake are
169 frequently subject to strong winds, which can last several hours to several days. However, the
170 eastern part of the lake is sheltered from strong winds by high mountains (Lemmin and
171 D'Adamo, 1996; Lemmin, 2020; Rahaghi et al., 2019).

172 The spatial pattern of the averaged *Bise* and *Vent* wind fields is shown in Figures 1c and
173 e. These strong uniform wind events can generate complex gyral flow pattern systems (Figures
174 1b and f). The surface currents in the lake's center are either cyclonic (counterclockwise
175 rotating) after a *Bise* wind or anticyclonic (clockwise rotating) after a *Vent* event (Hamze-Ziabari
176 et al., 2022a; Lemmin, 2016). In order to monitor the longterm water quality development of the
177 lake, the Commission Internationale pour la Protection des Eaux du Léman (CIPEL) has
178 measured physical and biological parameters regularly since 1967 at station SHL2 (Figure 1a).



179
 180 **Figure 1.** (a) Lake Geneva and surrounding topography, adapted from a public domain satellite
 181 image ([NASA World Wind](#), last accessed 13 December 2022) and bathymetry data from
 182 [SwissTopo](#) (last accessed 13 December 2022). The colorbar indicates the water depth. SHL2
 183 (yellow cross) is a long-term CIPEL monitoring station where physical and biological parameters
 184 are measured; red square: location of the EPFL Buchillon meteorological station (100-m
 185 offshore). The thick red arrows indicate the direction of the two strong dominant winds, called
 186 *Bise*, coming from the northeast and *Vent*, from the southwest. (b) Average wind speed and

187 direction during the *Bise* event that lasted from 18 to 20 September 2019. (c) Magnitude of
188 simulated near-surface current velocity patterns one day after the *Bise* ceased. A cyclonic gyre
189 formed in the center (widest part) of the *Grand Lac* basin of the lake (red circular arrow). (d)
190 Average wind speed and direction during the *Vent* event that lasted from 24 to 30 September
191 2019. (e) Near-surface (simulated) flow patterns one day after the *Vent* ceased. An anticyclonic
192 gyre formed in the center (widest part) of the *Grand Lac* basin (red circular arrow). Colorbars
193 indicate the range of the parameters.

194 2.2 Numerical simulations

195 We investigated the 3D processes involved in pelagic upwelling using the Massachusetts
196 Institute of Technology general circulation model (MITgcm). This code solves the 3D
197 Boussinesq, hydrostatic Navier-Stokes equations, including the Coriolis force (Marshall et al.,
198 1997). We applied the model setup of Cimadoribus et al. (2018, 2019) who calibrated the model
199 for Lake Geneva and demonstrated that stratification, mean flow and internal seiche variability
200 can be realistically simulated. In addition, Foroughan et al. (2022), Hamze-Ziabari et al. (2022a,
201 2022b) and Reiss et al. (2020, 2022) showed that the model can accurately capture both
202 submesoscale and basin/mesoscale processes in Lake Geneva. Realistic atmospheric fields
203 (including wind, temperature, humidity, solar radiation), extracted from the COntortium for
204 Small-scale MOdeling (COSMO) atmospheric model provided by MeteoSwiss with a resolution
205 of 1 km (Voudouri et al., 2017), were used to force the lake surface. Two Cartesian grids, a Low
206 Resolution (LR) grid (horizontal resolution 173 to 260 m, 35 depth layers) and a High Resolution
207 (HR) grid (horizontal resolution 113 m, 50 depth layers), were applied. The LR model was
208 initialized from rest using the temperature profile from the CIPEL SHL2 station (CIPEL, 2018)
209 measured on 19 December 2018 (calm weather conditions prevailed on this date). The LR model
210 spin-up was ~180 d. Note that the LR results were only used to initialize the HR model. The
211 layer thicknesses in the HR model ranged from 0.30 m at the surface to approximately 12 m for
212 the deepest layer and the integration time was 6 s.

213 2.3 Remote sensing

214 The signatures of coastal and pelagic upwelling in lakes and oceans are usually detected
215 using infrared and optical sensors. Advanced Very High-Resolution Radiometer (AVHRR) data
216 from the National Oceanic and Atmospheric Administration (NOAA) and the European
217 Meteorological Operational (MetOp) polar-orbiting satellites, which are routinely collected by

218 the Remote Sensing Research Group at the University of Bern (Riffler et al., 2015), were used to
219 study the spatial variability of pelagic upwelling events in Lake Geneva. AVHRR data have a
220 spatial resolution of 1.1 km at nadir and a temporal resolution of one to ten images per day
221 (Rahaghi et al., 2018; Bouffard et al., 2018). Detailed information is provided by Hüsler et al.
222 (2011) and Riffler et al. (2015).

223 2.4 In situ data

224 It was previously shown that gyre patterns in Lake Geneva can be reliably predicted by
225 numerical modeling based on forecasted COSMO meteo data (Hamze-Ziabari et al., 2022a).
226 Guided by these numerical model forecasts, one or more transects for field measurements were
227 selected within the main cyclonic gyre in the central part of the *Grand Lac* basin. Ten 1 km-
228 spaced profiles were measured along the transect. An ADCP (Acoustic Doppler Current Profiler,
229 Teledyne Marine Workhorse Sentinel) equipped with a bottom-tracking module was used to
230 measure the vertical profiles of current velocity at each point for at least 10 min. The ADCP was
231 set up for 100 1-m bins (blanking distance of 2 m). The transducer was located at 0.5 m depth,
232 and the high-resolution processing mode was chosen. Tilt and heading angles were derived from
233 an in-built sensor.

234 Vertical profiles of water temperature were measured with a multiparameter probe Sea
235 and Sun Marine Tech CTD75M and CTD90M at predefined points during the field campaigns.
236 The Conductivity Temperature Depth (CTD) instrument was lowered at $\sim 10 \text{ cm s}^{-1}$ and recorded
237 at 7 Hz, resulting in a sampling resolution of $\sim 1.5 \text{ cm}$.

238 2.5 Empirical Orthogonal Functions

239 Empirical Orthogonal Function (EOF) analysis is widely used to identify latent spatial
240 patterns in a dataset and how they change over time (Wang & An, 2005). In an EOF analysis,
241 similar to Fourier or wavelet analysis, the original dataset is projected onto an orthogonal base.
242 This orthogonal base is computed based on the eigenvectors of a spatially-weighted anomaly
243 covariance matrix. The associated eigenvalues are a measure of the variance captured by each
244 pattern. A thermocline with a dome- or bowl-shaped structure associated with pelagic upwelling
245 and downwelling, respectively, produces a coherent structure in the temperature field. The

246 spatial variability of pelagic upwelling can therefore be determined from EOFs of temperature in
 247 the thermocline layer.

248 2.6 Ekman pumping velocity

249 Wind-driven upwelling can occur in both coastal and offshore areas of lakes and oceans.
 250 In coastal upwelling, surface waters are transported away from the alongshore direction due to
 251 Ekman transport. This generates nearshore divergence in the surface layers, which is balanced by
 252 the upwelling of colder waters from below (Reiss et al., 2020). Upwelling in offshore areas can
 253 be caused by the divergence of Ekman mass transport, which results from the curl of the wind
 254 stress. The Ekman pumping velocity w induced by wind stress is given by (Bravo et al., 2016;
 255 Pickett & Paduan, 2003):

$$w = \frac{\nabla \times \tau}{\rho f} \quad (1)$$

256 where w is the Ekman pumping velocity, τ is the wind stress, ρ is the water density and f is the
 257 Coriolis frequency. The wind stress at the air-water interface was calculated from hourly
 258 COSMO data as:

$$\tau = (\tau_x, \tau_y) = \rho_a C_D \Delta \vec{U} |\Delta \vec{U}| \quad (2)$$

259 where τ_x is the zonal and τ_y is the meridional wind stress, $\Delta \vec{U} = \vec{U}(z_u) - \vec{U}_0$ is the difference
 260 between wind velocity vector at height z_u (typically 10 m) and the surface current. The drag
 261 coefficient at the air-water interface (C_D) was estimated as (Large & Yeager, 2004):

$$C_D (\times 10^3) = \frac{2.7}{U_{10N}} + 0.142 + 0.076 U_{10N} \quad (3)$$

262 where U_{10N} is the 10-m neutral-stability wind speed.

263 **3 Results**

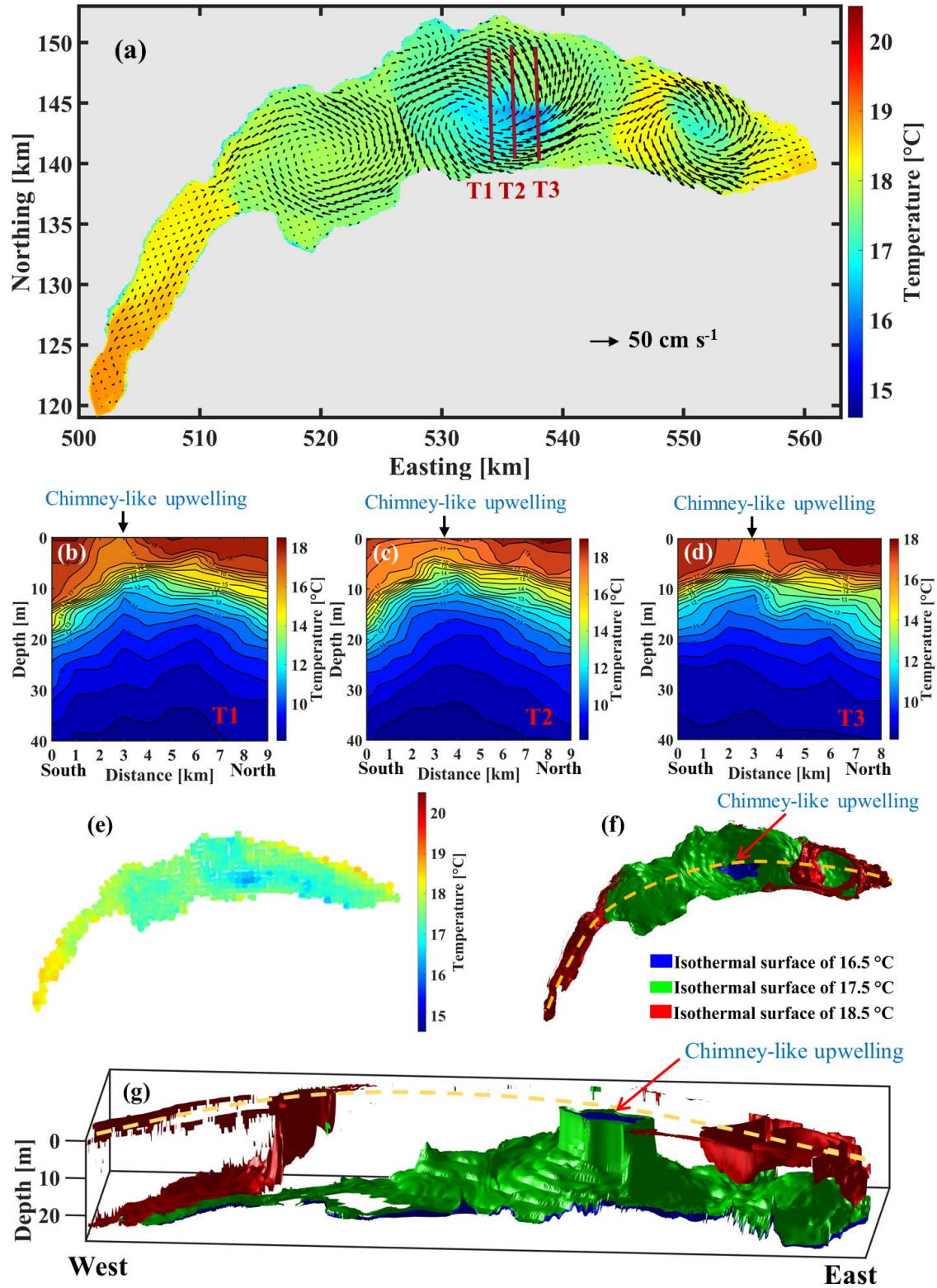
264 3.1 Field observations

265 This study focuses on *Bise* wind events that caused the formation of a cyclonic gyre and
266 pelagic upwelling in the central part of the *Grand Lac* basin of Lake Geneva. Pelagic upwelling
267 is important for the ecological development of the lake, since it transports nutrients from the
268 deeper layers into the phototrophic zone. Emphasis was put on cases where modeling suggests
269 that thermocline waters reach the surface. On 21 September 2019, a field measurement campaign
270 was carried out in the *Grand Lac* basin whose primary objective was to capture the dynamics of
271 the largest and most energetic basin-scale gyre in the center of the basin. A strong *Bise* event
272 started at 20:00 (CET) on 17 September 2019 and ended at 13:00 on 20 September 2019. The
273 mean wind speed was 3.65 m s^{-1} (mean wind gust 7.69 m s^{-1}) with a standard deviations of 0.86
274 m s^{-1} (gust standard deviation of 1.78 m s^{-1}). Details of the wind field are given in Figures 1b and
275 S1. As shown in Figure 2a, this wind event produced three basin-scale gyres. Three transects in
276 the central gyre, T1, T2 and T3, spaced at $\sim 1.8\text{-}2 \text{ km}$ distance (east to west), were pre-selected.
277 Each transect consisted of 10 profiles with 1-km spacing (Figure 2a). Temperature profiles at
278 each point were measured down to 40 m depth, i.e., the base of the thermocline.

279 The velocity field shows a cyclonic gyre (Figure 3). The maximum horizontal water
280 velocity reached $\sim 35 \text{ cm s}^{-1}$ in the near-surface layer. The upwelling in the center of the gyre was
281 accompanied by a strong reduction of the horizontal velocity, which can be clearly observed in
282 all transects. The gyre velocity field depth was slightly less than 15 m due to strong thermal
283 stratification (Figure 2b-d). However, the gyre affected the temperature profiles down to a depth
284 of $\sim 40 \text{ m}$. At depths below 10 m, the expected dome-shaped thermocline is evident in the
285 temperature profiles (Figure 2b). It was observed that the cyclonic gyre circulation pushes the
286 water from a depth of 10 m to the surface. As a result, the surface water temperature in the
287 center of the gyre is $1\text{-}1.5^\circ\text{C}$ colder than the surrounding surface water, as seen in the T1 and T2
288 transects. Below, we refer to these vertical cold water columns (e.g., between distances 2-3 km in
289 Figure 2b) as chimneys. These gyre features have apparently not been documented previously in
290 lakes/oceans in such detail.

291 The lake surface water temperature field retrieved from the Advanced Very High-Resolution
292 Radiometer (AVHRR) data with a spatial resolution of 1.1 km taken at 9:00 on 21 September 2019

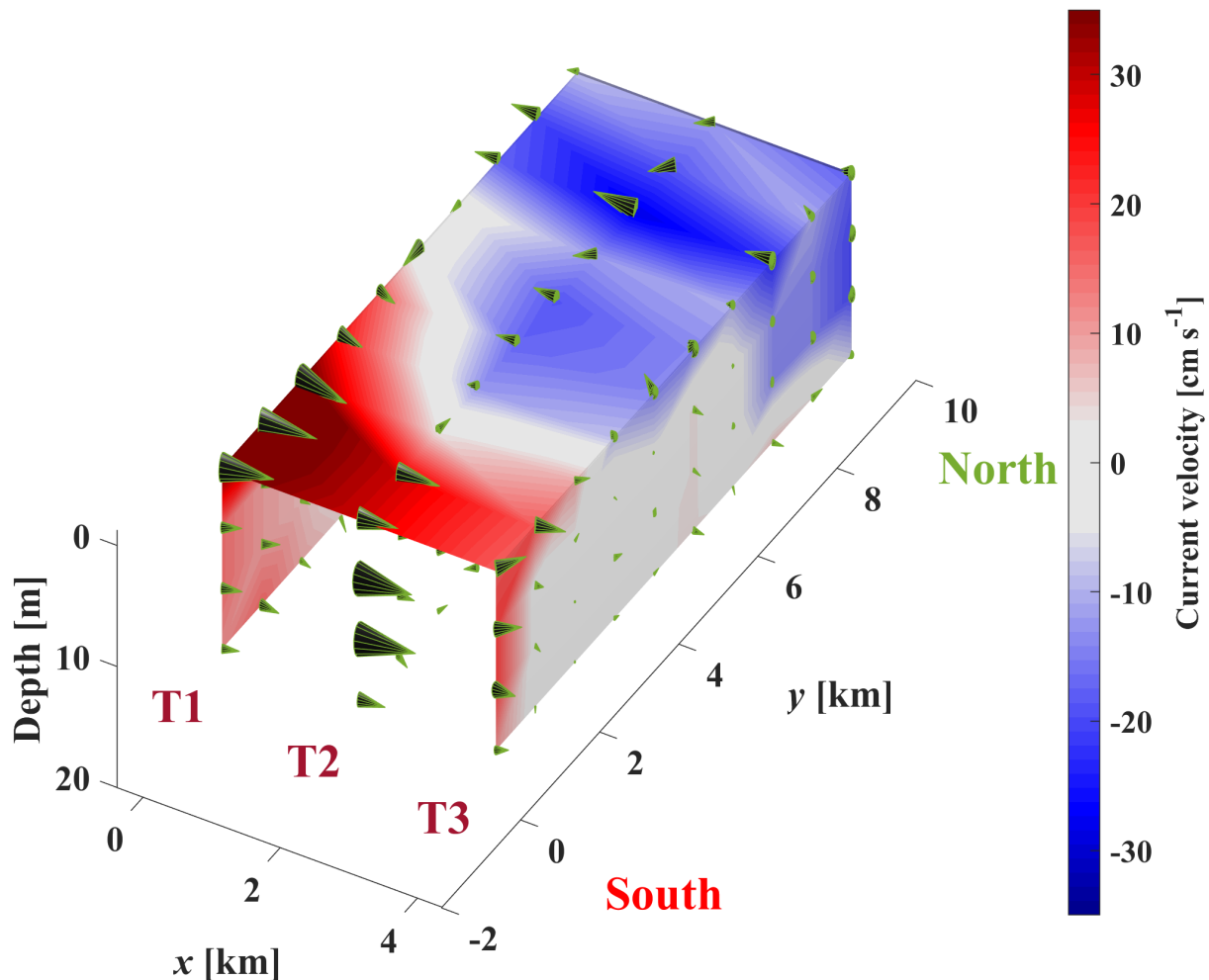
293 (Figure 2e) shows an irregular ellipse-like cold area that is 1°C colder than the surrounding surface
294 waters. The width of the ellipse is ~ 3 km and its length is ~ 5 km. A similar cold water pattern at
295 the same location with the same surface area is evident in the numerical results (Figure 2a),
296 indicating that the model predicts well the observations. The 3D structure of the pelagic upwelling
297 in the SML is illustrated by three isothermal surfaces of thermocline water at depths 10, 15 and 20
298 m in the nearshore areas (Figure 2f and g). In the center of the observed cyclonic gyre, the water
299 from the thermocline reaches the surface and forms a chimney-like structure in the SML (Figure
300 2g). The 3D structure of isothermal surfaces related to these upwelling zones is consistent with the
301 field measurements (Figure 2b-d), thus confirming the existence of a cold chimney-like structure
302 in the epilimnion layer, in which cooler water originating from the thermocline is transported
303 upwards into the surface layer.



304

305 **Figure 2.** (a) Numerical results of the temperature (colors; see colorbar) and velocity (arrows;
 306 see reference arrow) fields (0.3-m depth) for 21 September 2019 after the strong *Bise* wind

307 event, showing two cyclonic gyres, in the center and to the east, and one anticyclonic gyre in the
 308 western part of *Grand Lac* basin. The red lines in the central cyclonic gyre mark the predefined
 309 transects (T1, T2, T3) for the field campaign. (b-d) Contour plots based on the measured
 310 temperature profiles at T1, T2 and T3, respectively. Colorbar gives the temperature range. (e)
 311 AVHRR image taken on 21 September 2019 at 8:21 with the same temperature range as in panel
 312 (a). The location of the cold temperature ellipse in the center (blue) coincides well with the one
 313 predicted by the numerical modeling (panel a). (f) and (g) 3D structure of three isothermal
 314 surfaces related to the upwelling zones in the numerical results. Isothermal surfaces of
 315 thermocline water which have depths 10, 15 and 20 m in the nearshore areas are considered;
 316 compare with panels (b-d). (f) plane view. (g) side view. Yellow dashed line in (f) indicates the
 317 central plane orientation in (g). Orange arrows in (f) and (g) mark the location of the pelagic
 318 upwelling in the center of the cyclonic gyre in the *Grand Lac* basin.

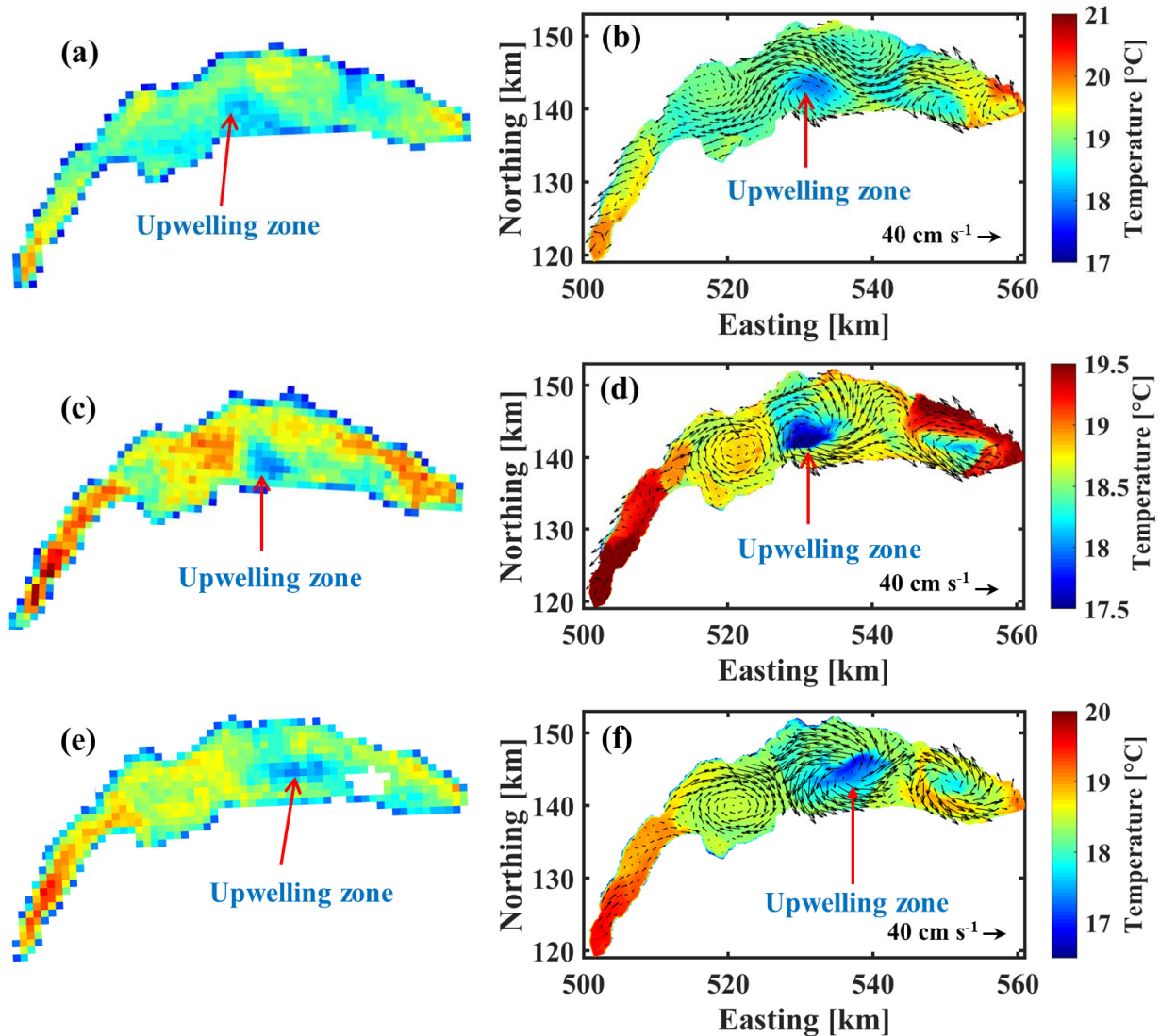


319 **Figure 3.** 3D structure of the cyclonic gyre velocity field based on the ADCP profiles taken
 320 during the field campaign of 21 September 2019 along transects T1, T2 and T3 shown in Figure
 321

322 2a. The size of the arrows is scaled with the current velocity. Contours show the current
323 velocities near the surface and on the sides of the investigated volume. Colorbar gives the range.

324 3.2 Evolution of spatial variability of pelagic upwelling during strong stratification

325 AVHRR data and numerical results are used to show the spatial variability of pelagic
326 upwelling over the lifetime of the gyre observed in September 2019 (Figure 4). In the AVHRR
327 images taken from 19 to 21 September 2019, it is evident that the location of pelagic cold areas
328 and their geometric shape are quite variable in time. The same spatial variability of the pelagic
329 upwelling can be seen in the corresponding numerical results, indicating reasonable agreement
330 with AVHRR data. On 19 and 20 September, the velocity fields in the numerical modeling
331 present a gyre-like pattern located in the South (Figure 4b, d). On 21 September, the modeled
332 gyre velocity field was fully developed and nearly symmetrical with respect to the center of the
333 lake with the cold upwelling zone also shifting towards the lake center. The AVHRR and
334 numerical results indicate that the cold surface areas correspond to the gyre's center, whose
335 location varies throughout its evolution. The simulated daily evolution of the gyre velocity field
336 in the near-surface layer during the September 2019 event is shown in Figure S2. Similar to
337 Figure 4, the location of the gyre center and the associated pelagic upwelling follow the
338 evolution of the gyre velocity field (Figure S3a). Note that on 20 and 21 September, a cyclonic
339 gyre in the East and anticyclonic gyre in the West of the *Grand Lac* basin are well developed.
340 For details of this three-gyre pattern, see Hamze-Ziabari et al. (2022a).



341
 342 **Figure 4.** Left column: AVHRR images. Right column: Corresponding simulated temperature
 343 (color contours) and near-surface velocity (black arrows) at 0.3 m depth. (a) and (b) for 19
 344 September 2019. (c) and (d) for 20 September 2019. (e) and (f) for 21 September 2019. Note that
 345 the AVHRR images and corresponding numerical results have identical colorbars.

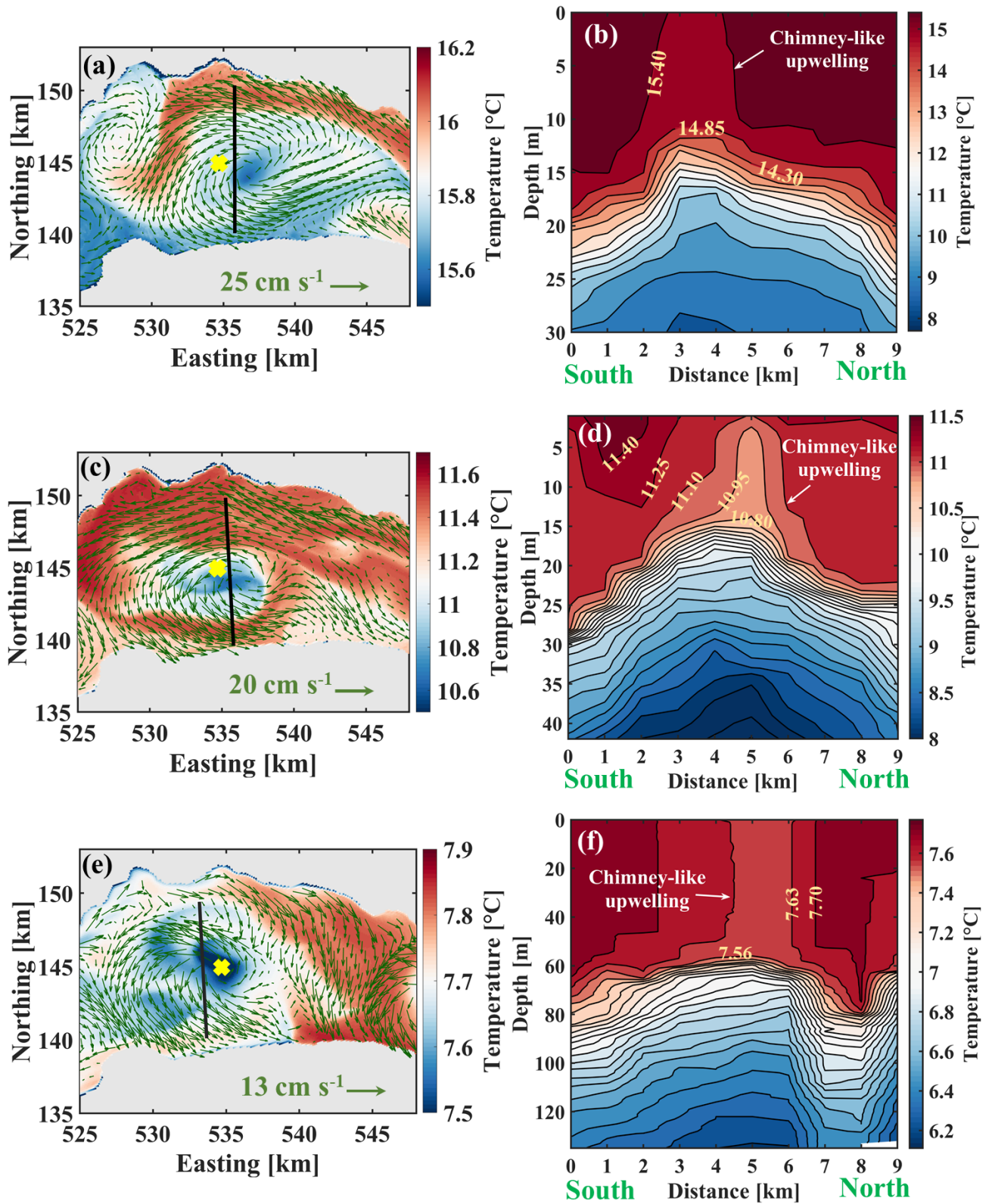
346 3.3 Chimney-like upwelling observations during weakly stratified seasons

347 During autumn and winter, colder air temperatures accompanied by stronger wind events
 348 erode the strong thermal stratification produced in the summer and move the thermocline down
 349 to greater depth in Lake Geneva. As a result, the gyre velocity field can likewise penetrate to
 350 greater depths, and thus can affect the strength and the depth of pelagic upwelling. To investigate
 351 the effect of seasonal changes, three field campaigns were carried out, each after a strong *Bise*

352 event in October 2019, November 2019 and January 2020. The wind speed and direction for
353 each event are shown in Figure S1. According to the numerical results, a cyclonic gyre is formed
354 after each of these wind events (Figure 5), and the cold upwelling zone can again be seen near
355 the lake surface, even though the thermocline is (much) deeper than in September 2019 (Figure
356 4). During these three field campaigns, the surface water temperatures at the center of transects
357 were, respectively, 0.4, 0.6 and 0.25°C lower than the ambient water temperature, and were equal
358 to nearshore water temperatures at depths of ~15, 25 and 70 m, measured at both ends of the
359 transects. These observations suggest that these chimney-like upwelling events, which have not
360 been reported before, are probably common features, and that their potential effect on different
361 processes in lakes should be considered.

362 Despite the high spatial variability of the upwelling zone during the lifetime of a cyclonic
363 gyre, model results and satellite imagery indicate that the pelagic upwelling can reach right up to
364 the lake surface. Based on numerical results, the chimney-like pattern of dense water can persist
365 for days to weeks. For example, the chimney-like upwelling lasted for almost 5 and 11 d,
366 respectively, for the September 2019 and January 2020 events (Figures S2-S4). The occurrence
367 and duration of chimney-like upwelling in the center of the lake are determined by the preceding
368 and subsequent strong wind events. More details about the lifetime and the effect of wind on the
369 September 2019 and January 2020 events are given in Text S1 and Figures S3 and S4.

370



371

372

373

Figure 5. Left column: Numerical results of near-surface velocity (green arrows) and temperature (color contours) for the cyclonic gyre in the center of the *Grand Lac* basin. Right

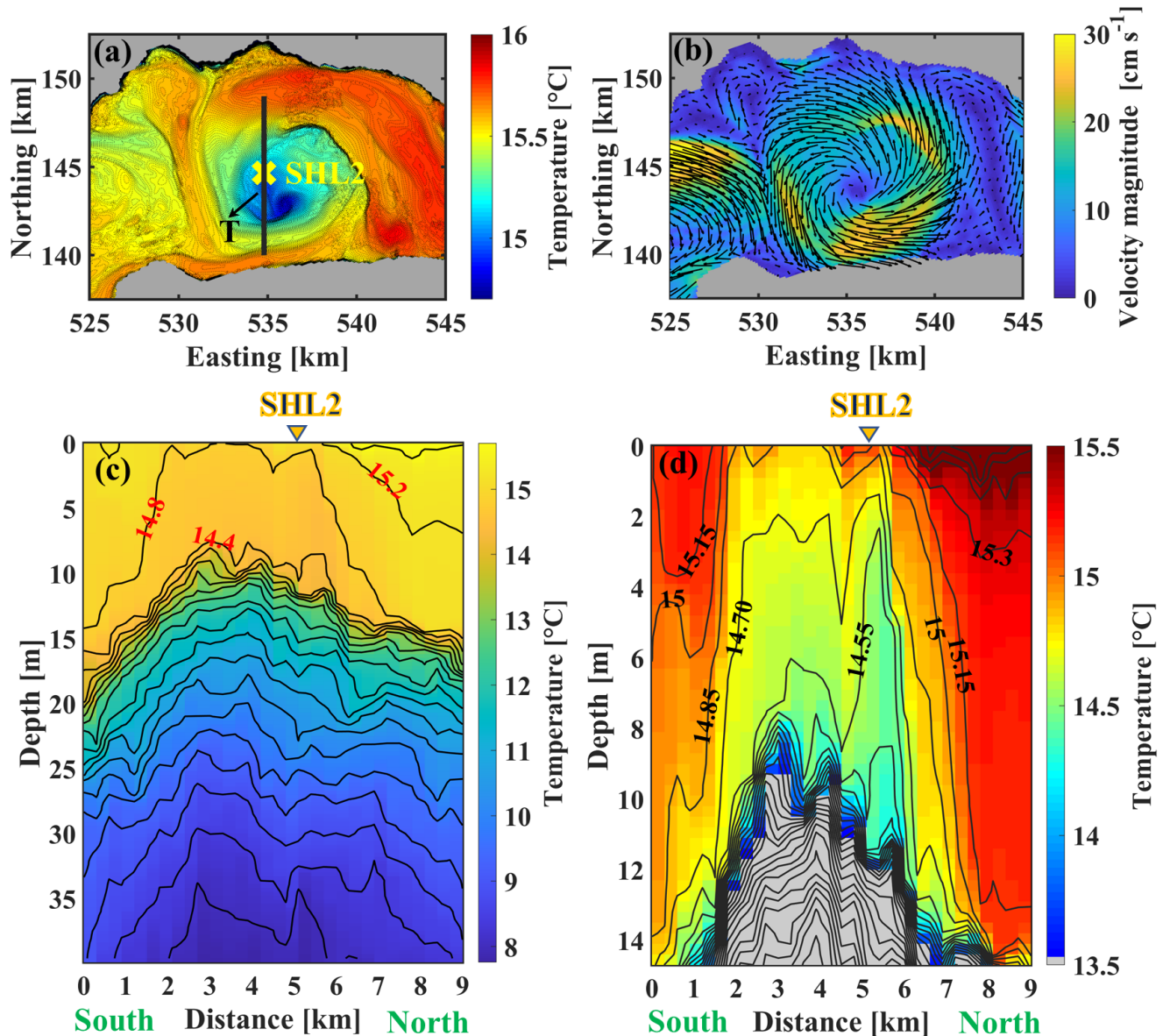
374 column: Field observations of chimney-like upwelling in the measured temperature profiles
375 along transects (black line in left panels) under weakly stratified conditions. (a) and (b) for 25
376 October 2019. (c) and (d) for 25 November 2019. (e) and (f) for 27 January 2020. The yellow
377 cross in the left panels indicates the location of SHL2 station. Colorbars give the temperature
378 range.

379 3.4 Chimney-like upwelling versus submesoscale filaments

380 Submesoscale cold filaments, i.e., narrow bands of cold water in the near-surface layer,
381 are ubiquitous inside cyclonic and anticyclonic gyres and eddies. The vertical structure of cold
382 filaments appears as a column of well-mixed cold water in the epilimnion layer. For example,
383 Hamze-Ziabari et al. (2022b) showed that cold submesoscale filaments with a width ranging
384 from 0.1 to 1 km can be formed at the edges and in the centers of the cyclonic gyres in Lake
385 Geneva. It was suggested that the pelagic upwelling at the center of the lake might provide the
386 buoyancy gradient required for filamentogenesis or frontogenesis (Gula et al., 2014;
387 McWilliams, 2019). A field campaign was conducted on 16 October 2021 after a strong *Bise*
388 event in order to distinguish between submesoscale filaments and chimney-like upwelling. The
389 spatial resolution of measurements was set at 300 m to capture submesoscale and mesoscale
390 patterns within cyclonic gyres. The location of transect T, which consisted of 30 measurement
391 points, was chosen based on the numerical forecast shown in Figure 6a.

392 The measured temperature profiles along transect T are plotted in Figure 6c. A dome-
393 shaped thermocline and a chimney-like upwelling in the mixed layer were observed (Figures 6c,
394 d). The chimney-like upwelling structure has a width of nearly 4 km, which is much wider than
395 that of submesoscale filaments reported in the literature. On the other hand, a smaller cold
396 structure (at distances between 5-6 km in Figure 6d) with a width of less than 1 km can be
397 observed near the upwelling zone. A combination of the buoyancy gradient generated by a
398 chimney-like upwelling and the background straining flow field can lead to the isolation and
399 elongation of such filamentary patterns in the center of cyclonic circulations. Thus, a chimney-
400 like upwelling in the mixed layer is required for filament formation in the center of the gyre. Its
401 formation mechanism however is different than that of filamentogenesis/frontogenesis. Transect
402 T passes through the location of CIPEL monitoring station SHL2 (see Figure 1 for location),
403 where long-term data of different physical and biological parameters are collected. From Figure

404 6c, it is evident that measurements taken at SHL2 are affected by the pelagic upwelling as will be
 405 further discussed below.



406
 407 **Figure 6.** Numerical results of (a) temperature and (b) velocity fields at 1-m depth for the
 408 cyclonic gyre in the center of the *Grand Lac* basin on 16 October 2022. The black line in a)
 409 marks predefined transect T (for the field campaign) which passes through station SHL2 (yellow
 410 cross). (c) Isotherm pattern obtained from temperature profiles measured along T showing the
 411 dome-shaped thermocline and the chimney-like pelagic upwelling. (d) Zoomed isotherm pattern
 412 of temperature profiles in the epilimnion layer measured along T (subset of panel (c)). Note the

413 cold filament between 5 and 6 km in (d). The location of monitoring station SHL2 is indicated on
414 the top of the panels. Colorbar legends give the range of the parameters.

415 **4 Discussion**

416 This study, carried out in Lake Geneva, has made evident for the first time in a lake that
417 intense pelagic upwelling occurs in the center of a basin-scale cyclonic gyre. It was shown that
418 cold water which upwelled from the thermocline layer, frequently reached up to the surface, as
419 was confirmed by satellite images. Detailed field measurement campaigns revealed the existence
420 of a dome-shaped thermocline and the gyre current pattern that caused this chimney-like
421 upwelling to rise like a cylindrical vertical water column, as was predicted by theory. 3D
422 numerical modeling results agreed with these observations. Based on 3D numerical modeling
423 results, we will discuss below the processes that can or cannot cause and modify pelagic
424 upwelling. Furthermore, we will assess the effects of pelagic upwelling on biogeophysical
425 processes and the way in which their long-term monitoring at a fixed location and their
426 quantification based on these measurements may be affected by the presence of a pelagic
427 upwelling zone.

428 4.1 Cause of upwelling

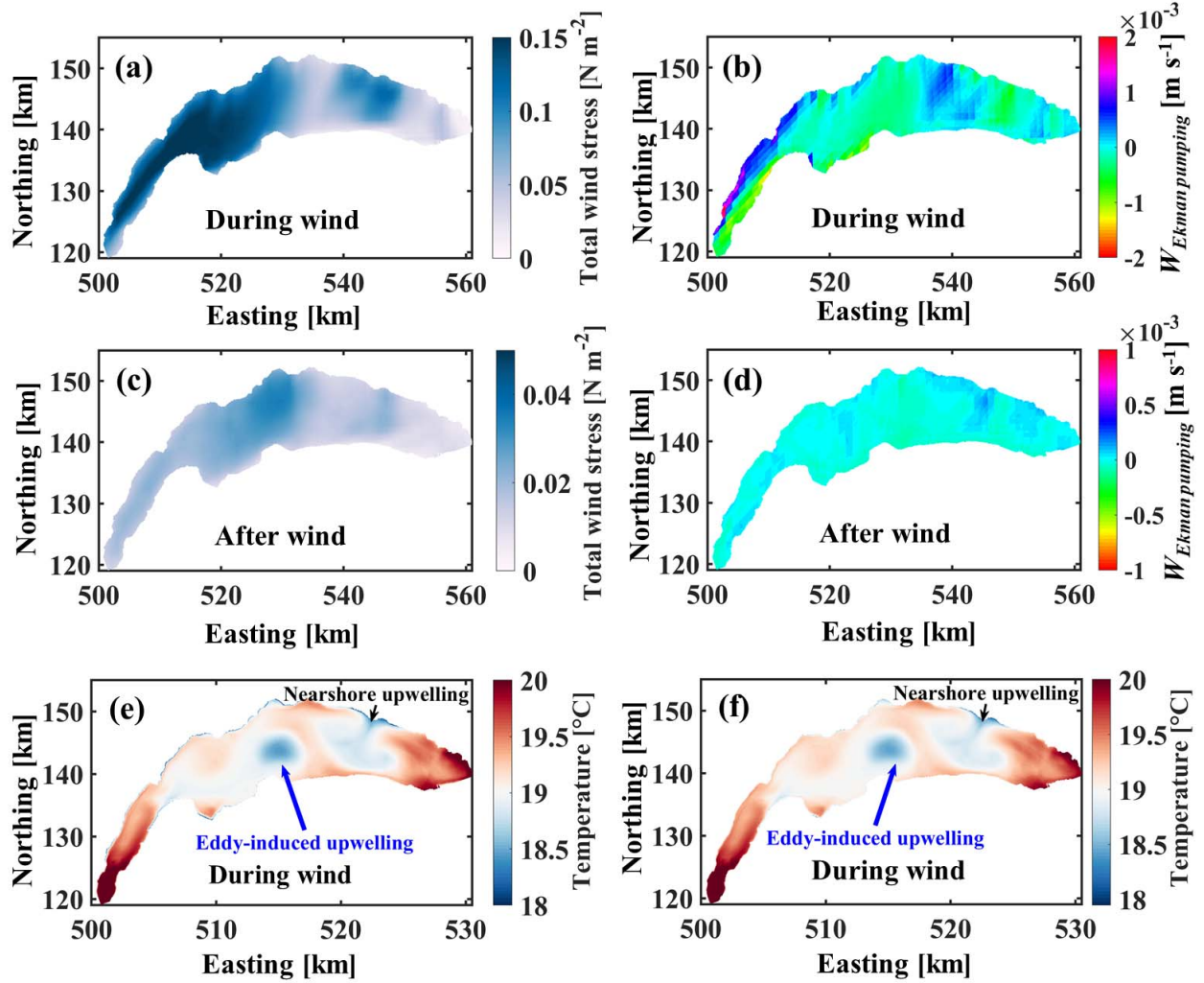
429 4.1.1 Ekman pumping

430 Ocean studies indicate that cyclonic winds can cause divergence of Ekman mass transport
431 in offshore areas, resulting in pelagic upwelling. For example, Lu et al. (2020) theoretically
432 demonstrated how Tropical Cyclones (TC) can cause vertical perturbations of the background
433 cyclonic and anticyclonic circulations. It was shown that the geostrophic responses to the TC
434 forcing can be divided into three layers: (i) the Ekman layer, (ii) an expansionary layer, and (iii)
435 a contractive layer. In the Ekman layer, a TC produces a chimney-like upwelling, accompanied by
436 an expansionary upwelling zone in the thermocline layer and, as depth increases, the Ekman
437 pumping decays. Although Ekman pumping had been proposed as a mechanism responsible for
438 pelagic upwelling in that study, there is little field evidence of its role in large lakes.

439 To understand the mechanism behind the observed chimney-like upwelling in Lake
440 Geneva, we first investigated the possibility of Ekman pumping based on numerical simulations
441 driven by COSMO wind data. Using daily-averaged wind stresses derived from COSMO, the

442 Ekman pumping velocities (Eq. 1) were calculated during and after the *Bise* event on September
443 2019 (Figures 1b and 7). Figures 7e and f display the daily average water temperature in the
444 near-surface layer and, at a depth of 15 m, respectively, during the *Bise* event. Two distinct cold
445 water zones are evident in the near-surface layers: (i) nearshore upwelling, and (ii) gyre/eddy-
446 induced upwelling. The nearshore upwelling corresponds to the area where the Ekman pumping
447 velocity is positive and maximum (Figure 7b). A similar nearshore upwelling pattern in the same
448 area is also seen in the AVHRR data (see Figure 4a). Nearshore upwelling has previously been
449 observed in Lake Geneva (Reiss et al., 2020). Comparing Figures 7e, f with Figures 7a, b and d,
450 it is obvious that the offshore Ekman pumping velocity resulting from wind stress curl is small
451 and negative and did not cause the eddy-induced cold-water pelagic upwelling zones in the
452 center of the lake. Ekman pumping can therefore be ruled out as the driver of the chimney-like
453 upwelling in the center of Lake Geneva.

454



455

456 **Figure 7.** The *Bise* wind event that lasted from 18 to 20 September 2019 and its effects. (a)
 457 Average wind stress and (b) estimated Ekman pumping velocity ($W_{Ekman\ pumping}$) during the *Bise*
 458 event. (c) Average wind stress and (d) estimated Ekman pumping velocity after the *Bise* event.
 459 (e) Daily average temperature in the near-surface layer at 0.3 m depth and (f) at 15 m depth
 460 during the *Bise* event. The colorbar legends indicate the range of the parameters.

461

4.1.2 Nonlinear dynamics associated with a cyclonic gyre

462

463

464

465

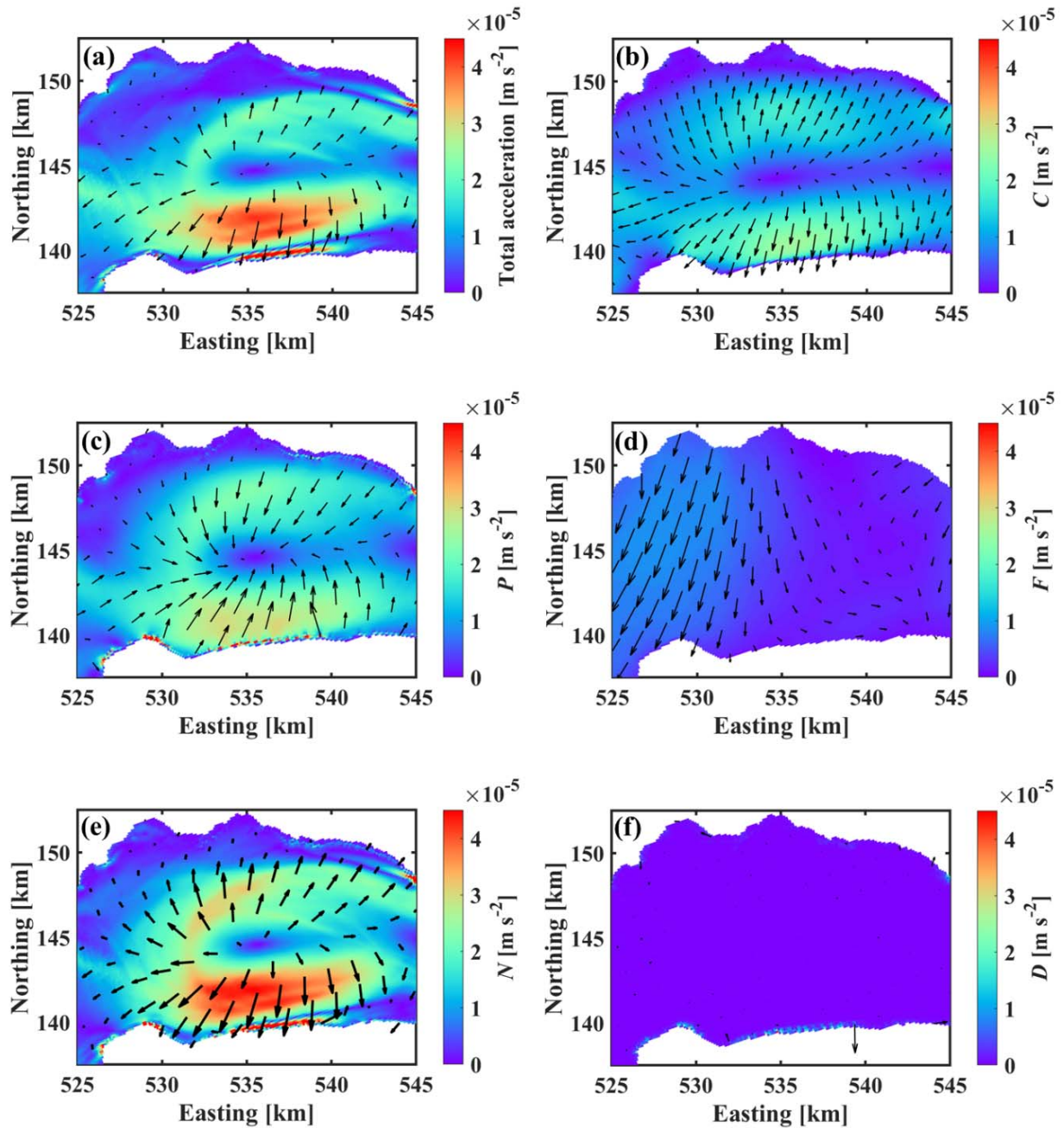
In order to investigate the dynamics of the gyre flow field in more detail, the effect of the different terms in the momentum equation are considered. For this, the vertically-averaged horizontal momentum equation over the depth layers influenced by the gyre velocity field (i.e., the thermocline layer and epilimnion) is expressed as (Cimatoribus et al., 2018; Vallis, 2017):

$$\frac{\partial U_h}{\partial t} = P + N + C + F - D \quad (4)$$

466 where U_h is the horizontal velocity field, P is the acceleration induced by the barotropic and
467 baroclinic pressure gradients, N is the acceleration caused by the nonlinear (advection) terms, C
468 is the acceleration caused by the Coriolis effect, F is the acceleration induced by the external
469 forces, and D is the deceleration due to dissipation (i.e., bulk, lateral, and bottom friction). First,
470 the mean zonal and meridional momentum trends caused by each term in the equation are
471 determined for the full lifetime of the gyre. The averaged spatial variability during the lifetime of
472 a cyclonic gyre in magnitude and the direction of the momentum trends induced by the different
473 terms are then examined. This analysis will be carried out for the September 2019 event for
474 which details of the dynamics are shown above (Figures 1c, 2, 3, 4).

475 The vertically (over ~ 30 m) and temporally (~ 6 d) averaged horizontal momentum trends
476 of the different terms in Eq. (4) for the cyclonic gyre that developed during the September 2019
477 event are illustrated in Figure 8. The resultant horizontal momentum acceleration trend indicates
478 a divergent pattern, as expected for a cyclonic gyre in the Northern Hemisphere (Figure 8a). In
479 the southern part of the gyre, the horizontal acceleration is much greater compared to the
480 northern part of the gyre. According to Figures 8b and c, the Coriolis and pressure terms act in
481 opposite directions. In the cyclonic gyre in the center of the *Grand Lac* basin, the Coriolis term
482 shows a divergent pattern, and the pressure term, a convergent pattern. The pressure effect is
483 slightly greater than the Coriolis effect, but is of the same order. The pressure term is the only
484 term that opposes the advective term. These two terms clearly cannot be responsible for the
485 resultant momentum acceleration pattern in terms of direction and magnitude. The external
486 forcing term is considerably less important than the Coriolis and pressure terms (Figure 8d).
487 Furthermore, there is no correlation between the patterns of local atmospheric forcing and the
488 resultant acceleration. The dissipation term is negligible compared to the other terms and is only
489 important in the nearshore zones (Figure 8f). The nonlinear (advective, Figure 8e) term,
490 however, exceeds the effect of all the other terms. It is of the same order as the resultant
491 momentum acceleration (Figure 8a), but slightly greater, compensated in part by the pressure
492 term. These results are in agreement with the early findings by Bohle-Carbonell & Lemmin
493 (1988), who showed that the nonlinear acceleration terms computed for Lake Geneva could be as
494 large or greater than the other terms. Thus, this nonlinear divergent nature of gyre dynamics can
495 be responsible for the formation of the observed intense chimney-like upwelling at its center.

496 The heterogeneous divergent flow shown in Figure 8a may also result in considerable horizontal
 497 strain in the gyre's center and around its periphery.



498 **Figure 8.** The contribution of different terms to the vertically (30 m) and temporally (6 d)
 499 averaged horizontal momentum equation for the September 2019 *Bise* wind event (Figure 1b),
 500 computed using Eq. (4). (a) Total acceleration, (b) Coriolis term, (c) Pressure term, (d) External
 501

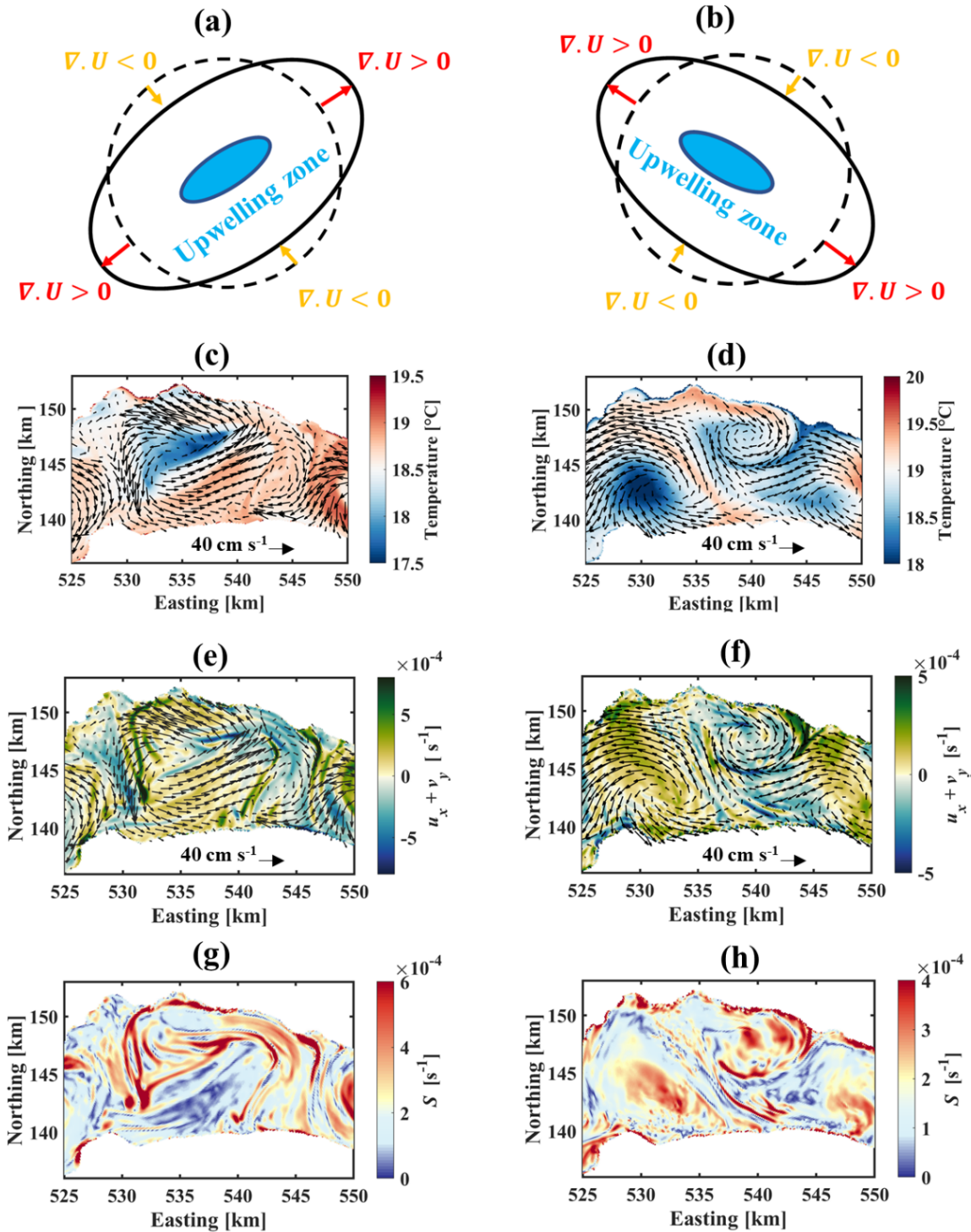
502 forcing, (e) Nonlinear (advective) term, and (f) Dissipative term. Arrows indicate the direction
 503 and intensity of the trend. Colorbars give the range of parameters.

504 4.1.3 Ageostrophic divergence and strain

505 Numerical results and AVHRR data (Figures 2 and 4) indicate that the gyre velocity field
 506 continuously changes as it develops, and the upwelling zone changes accordingly. Moreover, as
 507 shown in Figure 8, the nonlinear divergence dynamics associated with the gyre flow field can be
 508 spatially variable. In contrast to the ocean, a lake gyre velocity field is strongly affected by the
 509 morphology of its basin. For example, in long narrow lakes, such as Lake Geneva, there is a
 510 tendency for the gyre velocity field and the associated pelagic upwelling zone to form an
 511 elliptical pattern (e.g., Figure 2a). Furthermore, local winds and interactions with other large-
 512 scale currents can alter the gyre velocity field. Due to sudden changes in the gyre velocity field,
 513 divergence and strain fields within the gyre can be spatially variable.

514 A simplified conceptual diagram of the inward and outward distortions that can be caused
 515 by an elliptical velocity field is presented in Figures 9a, b. Conservation of mass dictates that an
 516 inward distortion along the minor axis of the ellipse leads to flow convergence. On the other
 517 hand, an outward distortion leads to flow divergence along the major axis. The center of a gyre
 518 can be subjected to high strain as a result of both inward and outward distortions. As an example,
 519 the divergence parameter, $\sigma = u_x + v_y$ (Figure 9e,f), and the horizontal strain rate, $S =$

520 $\sqrt{(u_x - v_y)^2 + (v_x + u_y)^2}$ (Figure 9g, h), computed at 1 m depth are shown for the September
 521 2019 *Bise* event. The corresponding upwelling patterns are quite different (Figures 9c, d). In
 522 general, flow divergence dominates the cyclonic gyre's velocity field. However, the sign of the
 523 divergence parameter can change at the edges and in the center of the gyre, due to the interaction
 524 with basin borders and other large-scale currents, and the constant distortions of the gyre's
 525 velocity field. According to Figures 9g and h, the distortion of the gyre velocity field results in a
 526 high horizontal strain rate inside the cyclonic gyre. It can be observed that the pelagic upwelling
 527 area is generally associated with high strain zones, and its shape is similar to that of the
 528 horizontal strain rate. There are, however, some areas of high strain that are not associated with
 529 cold water, such as the nearshore areas and the edges of the gyre where it interacts with other
 530 large-scale currents. Pelagic upwelling caused by gyres is therefore a 3D process, which cannot
 531 be studied solely on the basis of horizontal patterns of divergence and strain parameters.



532

533

534

535

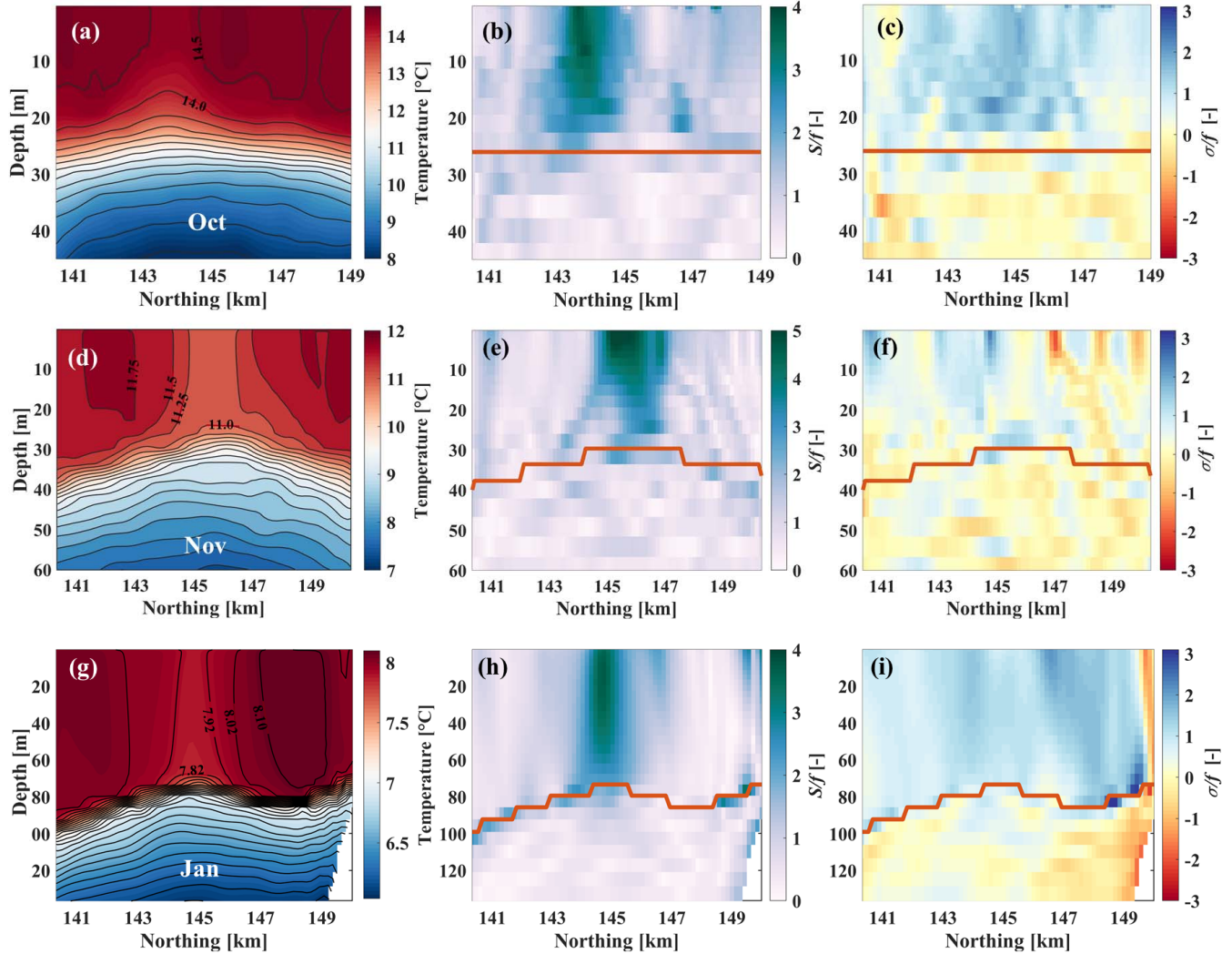
536

Figure 9. Two different velocity fields during the September 2019 *Bise* wind event caused by inward distortion (left column) and outward distortion (right column): (a) and (b) Schematic view of inward and outward distortion in an elliptical velocity field. (c) and (d) Simulated temperature at 2 m depth. (e) and (f) Computed divergence parameter. (g) and (h) Computed

537 horizontal strain rate, S . Colorbars give range of parameters. Black arrows indicate the near-
538 surface velocity fields.

539 The effects of heterogeneous divergence or convergence within the gyre flow field as
540 well as the strain caused by it were further investigated for the October, November, and January
541 field measurement campaigns along three transects (see Figure 5 for transect locations), where
542 chimney-like upwelling was detected (Figure 10). The chimney-like upwelling patterns observed
543 in the field and the simulated ones are in good agreement (Figures 5 and 10). The divergence
544 parameter indicates that the flow generally diverges in the mixed layer, whereas it converges in
545 the deeper layers below the zone of maximum stratification strength (red horizontal lines in
546 Figure 10). It appears that there is no direct correlation between the chimney-like upwelling in
547 the mixed layer and the flow divergence in the epilimnion. A high ageostrophic strain ($> f$, the
548 Coriolis frequency) zone is found in the epilimnion at the location where chimney-like
549 upwellings were observed (Figure 10). The higher strain rate extends from the near-surface down
550 to the thermocline layer and potentially stimulates ageostrophic perturbations (see Figure S5, as
551 an example, for hourly evolution of strain rate and chimney-like upwelling). The perturbed cold
552 thermocline water can be transported by the background divergence flow into the epilimnion.
553 This results in an upward flux of cold water from the thermocline layer, which is followed by a
554 chimney-like pelagic upwelling depending on the shape of the area imposed by the strain. Such
555 strong 3D ageostrophic strain accompanied by upwelling can increase the ageostrophic kinetic
556 energy, favor a higher chlorophyll growth rate, and enhance primary production (Zhang et al.,
557 2019).

558

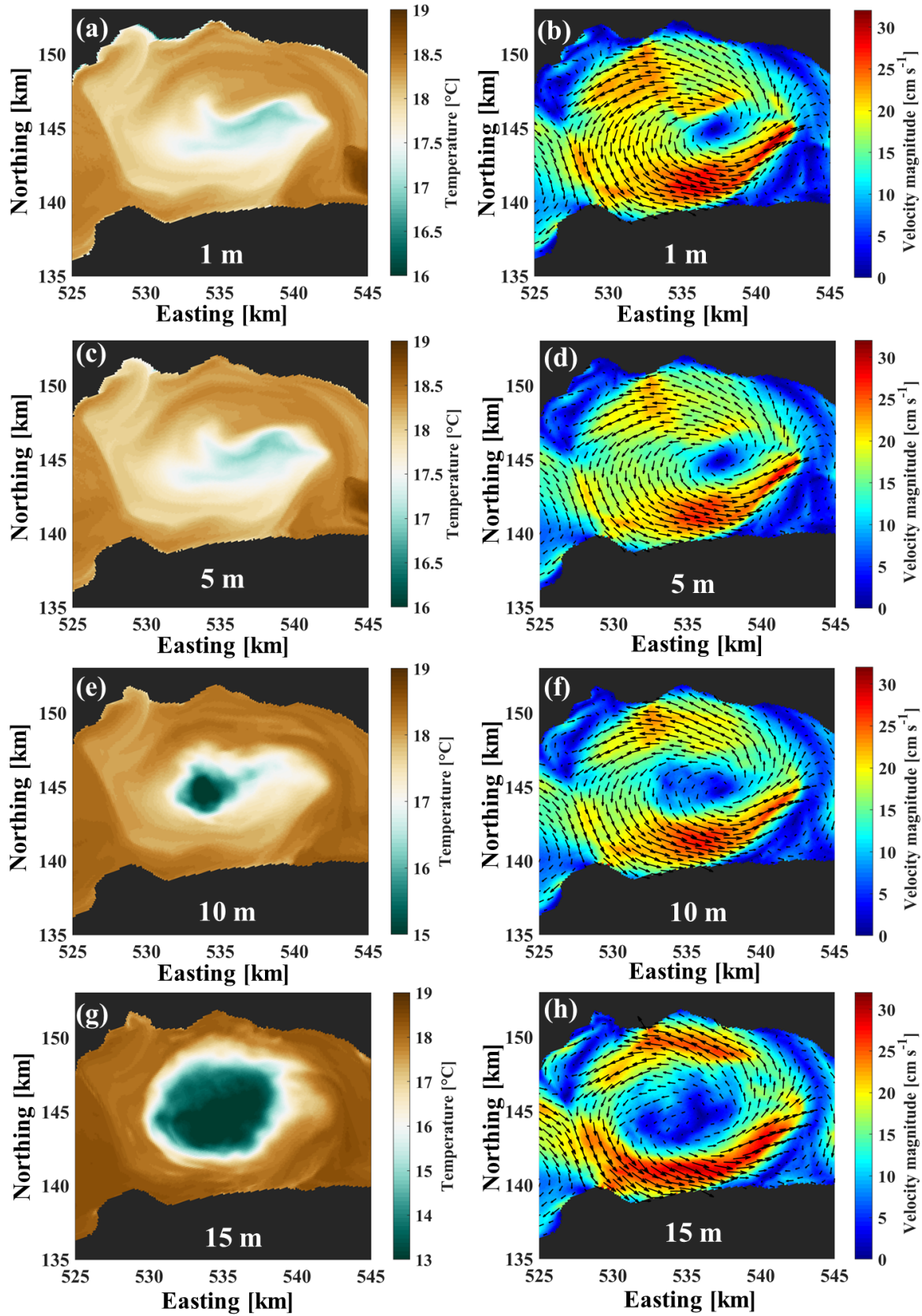


559

560 **Figure 10.** Simulated profiles of temperature (left column), horizontal strain rate (center
 561 column), and divergence parameters (right column) along the transects shown in Figure 5 for the
 562 (a-c) October 2019, (d-f) November 2019 and (g-i) January 2020 field campaigns. The red line
 563 indicates the zone of maximum stratification strength. Note that temperature ranges are different
 564 in (a), (d) and (g).

565 Several physical processes, such as lateral stirring, advection by the rotational velocity of
 566 gyres or eddies, and the translation of the gyre velocity field, can continuously alter the shape of
 567 the chimney of cold upwelled water in different depth layers (Lv et al., 2022). The gyre velocity
 568 is almost uniformly distributed in the deeper layers (e.g., 15 m depth) and the upwelling appears
 569 as a well-defined circular cold pattern (Figure 11). On the other hand, the gyre velocity field is
 570 spatially variable in the near-surface layers, primarily due to its nonlinear dynamics and its
 571 reaction to the constantly changing local atmospheric forcing conditions. Upwelling patterns,

572 therefore can differ considerably in different depth layers (Figure 11). In AVHRR images, cold
573 areas represent the superposition of upwelling patterns and other local physical processes.
574 AVHRR data on 21 September (Figure 4e), which correspond to the pelagic upwelling shown in
575 Figure 11, may therefore underestimate the area affected by the pelagic upwelling, in part due to
576 limited resolution.



577

578

Figure 11. Left column: Modeled distributions of temperature (indicating pelagic upwelling).

579 Right column: Gyre velocity field. (a) and (b) 1 m. (c) and (d) 5 m. (e) and (f) 10 m. (g) and (h)
580 15 m in the large-scale cyclonic gyre in the center of the *Grand Lac* basin of Lake Geneva for 21
581 September 2019. Colorbars indicate the range of the parameters. Note that the temperature
582 ranges in the left panels change. Arrows in right panels give velocity vectors.

583 4.2 Effect of thermocline shape on long-term observations at a fixed monitoring station

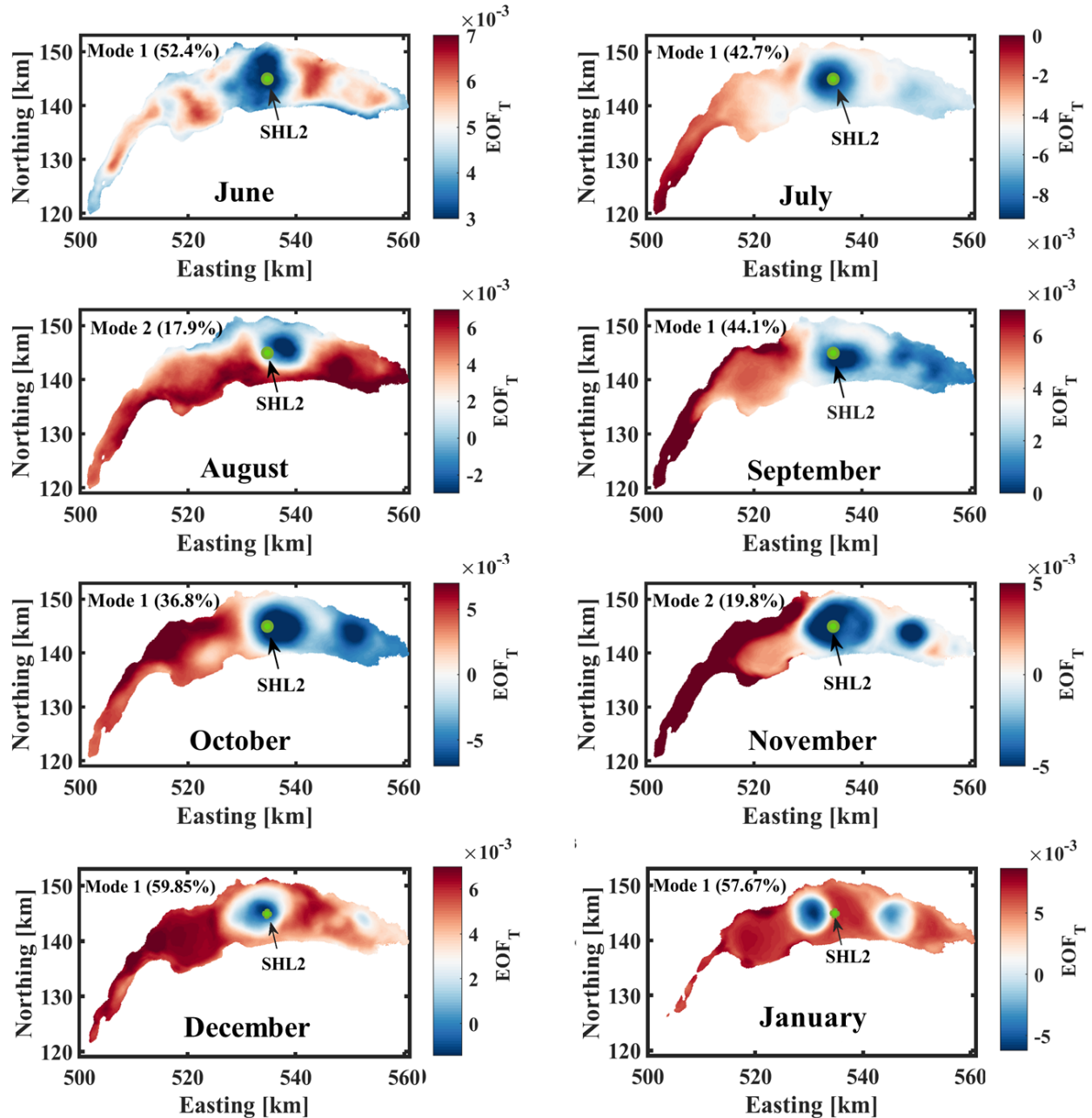
584 There is growing concern about the widespread reliance on single or few profile
585 measurements for monitoring and quantifying different processes in large lakes (Gaillard et al.,
586 2022). Vertical upward transport of thermocline water can have a significant impact on physical
587 and biological processes of a lake. A field study conducted in Lake Issyk-Kul revealed that the
588 dissolved oxygen level in the near surface layers of the pelagic upwelling zone can increase
589 (Romanovsky & Shabunin, 2002). In Lake Tanganyika an increase in nutrient concentrations and
590 phytoplankton chlorophyll levels were found in pelagic upwelling zones (Corman et al., 2010).
591 Primary production in upwelling areas is expected to increase as nutrient load increases (Jane et
592 al., 2021).

593 Long-term profile measurements taken at SHL2 (Figure 1) in Lake Geneva, for example,
594 are used by CIPEL to quantify various physical and biological processes in budget estimates to
595 determine longterm water quality development in the whole lake (e.g., CIPEL, 2018). The above
596 numerical results and field observations have made evident that station SHL2 is often located in
597 the pelagic upwelling zone of the cyclonic gyre in the center of the *Grand Lac* basin (e.g.,
598 Figures 5, 6). Thus measurements taken at that station may be affected by pelagic upwelling
599 dynamics.

600 To determine the structure of pelagic upwelling over a longer period, EOF analysis can
601 be used to compute the dominant spatial temperature variability. In EOF analysis, the signature
602 of upwelling/downwelling induced by cyclonic/anticyclonic circulations can appear as nearly
603 circular areas with temperatures that are different than the surrounding waters. Since the
604 signature of upwelling is more obvious in deeper layers and it is less regular near the surface due
605 to the high spatial variability of the upwelling zone and local external forces (Figure 11), the
606 EOF analysis was performed on the average temperature of the thermocline layer (Figure 12).
607 For each month, the depth of the thermocline layer was determined following Xu et al. (2019).
608 The results of the EOF analysis show that pelagic upwelling can be identified by a circular cold

609 water area in the center of the lake in all months (Figure 12). With the exception of August and
610 November 2019, the upwelling signature appears in the first mode.

611 During the study period from 1 June 2019 to 1 January 2020, pelagic upwelling modified
612 the temperature profile at the SHL2 location 41.5% of the time (101.5 d out of 245 d). Simulated
613 temperature profiles at the SHL2 location indicate that during this period, five out of twelve
614 SHL2 profiles may have been affected by pelagic upwelling caused by cyclonic gyres generated
615 by strong *Bise* events (Figure S6 and Text S2). Thus, care should be taken when developing
616 longterm concepts based solely on SHL2 measurements. Further research should be carried out
617 to determine the impact of pelagic upwelling on biological and chemical parameters and on
618 water quality in order to quantify the effect of pelagic upwelling on biogeochemical processes
619 and on measurements taken at single, fixed monitoring stations.



620
 621 **Figure 12.** Empirical Orthogonal Function (EOF) analysis of the average temperature in the
 622 thermocline layer for different months from June 2019 to January 2020; the month and dominant
 623 mode (% of occurrence) are indicated in each panel. The green circle marks the location of
 624 station SHL2 which most of the time is in the large-scale (dark blue) gyre area where pelagic
 625 upwelling occurs in the *Grand Lac* basin of Lake Geneva.

626 **5 Summary and Conclusions**

627 A unique combination of field measurements, 3D modeling, and satellite imagery
 628 allowed documenting for the first time in a lake (Lake Geneva), the frequent occurrence of

629 dome-shaped thermoclines and strong pelagic upwelling in the center of cyclonic basin-scale
630 gyres under different stratification conditions. Field measurement campaigns were designed
631 based on numerical modeling predictions, to capture pelagic upwelling in the presence of a
632 shallow, strong or a deep, weak thermocline. It was shown that:

- 633 • Pelagic upwelling forms chimney-like structures that can transport cold thermocline
634 water upwards to the epilimnion layer and frequently, even to the lake surface, as
635 confirmed in thermal (AVHRR) imagery and numerical simulations.
- 636 • The height of the chimney was about 10 to 20 m in September 2019 (shallow, strong
637 thermocline) and 60 to 80 m in January 2020 (deep, weak thermocline).
- 638 • According to the modeling results, the detected upwelling can persist for 5-11 days
639 depending on preceding and subsequent wind conditions.
- 640 • Neither the presence of wind stress over cyclonic circulations, nor wind stress curl was
641 observed in the upwelling zone during and after wind events. Numerical results indicate
642 that Ekman pumping cannot be responsible for the formation of this chimney-like
643 upwelling.
- 644 • The contribution of the terms of the momentum equation vertically-averaged over the
645 lifetime of a gyre, revealed that the nonlinear term is the dominant acceleration term. A
646 heterogeneous divergence flow formed around the pelagic upwelling zone due to the
647 influence of the advective acceleration.
- 648 • The heterogeneous divergence flow associated with the gyre flow field and the continuous
649 distortion of the gyre during its evolution produce an ageostrophic strain in the center of
650 the cyclonic gyre that can penetrate the thermocline layer, even a deep thermocline (~60-
651 80 m).
- 652 • Cold water was transported from the thermocline to the mixed layer and to the water
653 surface by the background divergence flow in the epilimnion layer. The cold-water areas
654 observed in the AVHRR images correspond to the areas affected by the chimney-like
655 upwelling; their shape is mainly determined by the horizontal strain field at the water
656 surface.

657 Large (basin-scale) cyclonic gyres are ubiquitous in Lake Geneva and other large lakes,
 658 which suggests that these newly discovered chimney-like pelagic upwelling events occur
 659 regularly and that they can affect the interplay of complex 3D biochemicalphysical processes
 660 occurring in lakes. Intense pelagic upwelling may, for example, impact on phytoplankton growth
 661 cycles due to the vertical redistribution of nutrients and potential pollutants. It can also affect
 662 routine single profile measurements taken at a fixed station if the station is located within the
 663 pelagic upwelling zone. Since long-term monitoring measurements are frequently used to
 664 evaluate the water quality status of the entire lake, the effect of pelagic upwelling can have
 665 severe consequences if lake management concepts are solely based on these measurements. The
 666 interplay of physical, biological and chemical processes within gyres and pelagic upwelling
 667 should be taken into consideration.

668 **Acknowledgments**

669 This research was supported by the Swiss National Science Foundation (SNSF Grant 178866).
 670 The spatiotemporal meteorological data were provided by the Federal Office of Meteorology and
 671 Climatology in Switzerland ([MeteoSwiss](http://www.meteo.ch)). We also extend our appreciation to the Commission
 672 Internationale pour la Protection des Eaux du Léman ([CIPEL](http://www.cipel.ch)) for in situ temperature
 673 measurements. Water temperature profiles were collected at the CIPEL SHL2 station for 2018-
 674 2019 by the Eco-Informatics ORE INRA Team at the French National Institute for Agricultural
 675 Research ([SOERE OLA-IS, INRA Thonon-les-Bains, France](http://www.soere-ola-is.inra.fr)).
 676

677 **Data availability**

678 The three-dimensional model used in this study is based on the MIT General Circulation Model
 679 (MITgcm, <http://mitgcm.org/>, <https://doi.org/10.1029/96JC02775>), which is publicly available.
 680 The data used in this manuscript will be uploaded to a Zenodo repository. For review purposes,
 681 the in situ data and numerical configurations supporting the findings of this study are available
 682 online at <https://github.com/mahmoodziabar/Data-for-Chimney-like-Upelling-in-Lake-Geneva>.
 683

684 **References**

- 685 Akitomo, K., Tanaka, K., Kumagai, M., & Jiao, C. (2009). Annual cycle of circulations in Lake
 686 Biwa, part 1: model validation. *Limnology*, *10*(2), 105–118.
 687 <https://doi.org/10.1007/s10201-009-0267-7>
- 688 Beletsky, D., & Schwab, D. (2008). Climatological circulation in Lake Michigan. *Geophysical*
 689 *Research Letters*, *35*(21), L21604. <https://doi.org/10.1029/2008GL035773>
- 690 Beletsky, D., Hawley, N., Rao, Y. R., Vanderploeg, H. A., Beletsky, R., Schwab, D. J., &
 691 Ruberg, S. A. (2012). Summer thermal structure and anticyclonic circulation of Lake
 692 Erie. *Geophysical Research Letters*, *39*(6), L06605.
 693 <https://doi.org/10.1029/2012GL051002>

- 694 Beletsky, D., Hawley, N., & Rao, Y. R. (2013). Modeling summer circulation and thermal
 695 structure of Lake Erie. *Journal of Geophysical Research: Oceans*, 118(11), 6238–6252.
 696 <https://doi.org/10.1002/2013JC008854>
- 697 Bennington, V., McKinley, G. A., Kimura, N., & Wu, C. H. (2010). General circulation of Lake
 698 Superior: Mean, variability, and trends from 1979 to 2006. *Journal of Geophysical
 699 Research: Oceans*, 115(C12), C12015. <https://doi.org/10.1029/2010JC006261>
- 700 Bohle-Carbonell, M., & Lemmin, U. (1988). Observations on non-linear current fields in the
 701 Lake of Geneva. *Annales Geophysicae*, 6(1), 89–100.
- 702 Bouffard, D., Kiefer, I., Wüest, A., Wunderle, S., & Odermatt, D. (2018). Are surface
 703 temperature and chlorophyll in a large deep lake related? An analysis based on satellite
 704 observations in synergy with hydrodynamic modelling and in-situ data. *Remote Sensing
 705 of Environment*, 209, 510–523. <https://doi.org/10.1016/j.rse.2018.02.056>
- 706 Brannigan, L. (2016). Intense submesoscale upwelling in anticyclonic eddies. *Geophysical
 707 Research Letters*, 43(7), 3360–3369. <https://doi.org/10.1002/2016GL067926>
- 708 Bravo, L., Ramos, M., Astudillo, O., Dewitte, B., & Goubanova, K. (2016). Seasonal variability
 709 of the Ekman transport and pumping in the upwelling system off central-northern Chile
 710 ($\sim 30^\circ$ S) based on a high-resolution atmospheric regional model (WRF). *Ocean Science*,
 711 12(5), 1049–1065. <https://doi.org/10.5194/os-12-1049-2016>
- 712 Cimatoribus, A. A., Lemmin, U., Bouffard, D., & Barry, D. A. (2018). Nonlinear dynamics of
 713 the nearshore boundary layer of a large lake (Lake Geneva). *Journal of Geophysical
 714 Research: Oceans*, 123(2), 1016–1031. <https://doi.org/10.1002/2017JC013531>
- 715 Cimatoribus, A. A., Lemmin, U., & Barry, D. A. (2019). Tracking Lagrangian transport in Lake
 716 Geneva: A 3D numerical modeling investigation. *Limnology and Oceanography*, 64(3),
 717 1252–1269. <https://doi.org/10.1002/lno.11111>
- 718 CIPEL. (2018), Rapports sur les études et recherches entreprises dans le bassin lémanique,
 719 Campagne 2017. Commission internationale pour la protection des eaux du Léman
 720 (CIPEL), Nyon, Switzerland. [Reports on studies and research undertaken in Lake
 721 Geneva (Léman) accessed 15 Sept. 2019]. Available from [http://www.cipel.org/wp-
 722 content/uploads/2018/04/RapportScientifique_camp_2016_VF.pdf](http://www.cipel.org/wp-content/uploads/2018/04/RapportScientifique_camp_2016_VF.pdf).
- 723 Corman, J. R., McIntyre, P. B., Kuboja, B., Mbemba, W., Fink, D., Wheeler, C. W., et al. (2010).
 724 Upwelling couples chemical and biological dynamics across the littoral and pelagic zones
 725 of Lake Tanganyika, East Africa. *Limnology and Oceanography*, 55(1), 214–224.
 726 <https://doi.org/10.4319/lo.2010.55.1.0214>
- 727 Csanady, G. T. (1968). Wind-driven summer circulation in the Great Lakes. *Journal of
 728 Geophysical Research (1896-1977)*, 73(8), 2579–2589.
 729 <https://doi.org/10.1029/JB073i008p02579>
- 730 Csanady, G. T. (1973). Wind-induced barotropic motions in long lakes. *Journal of Physical
 731 Oceanography*, 3(4), 429–438. [https://doi.org/10.1175/1520-
 732 0485\(1973\)003<0429:WIBMIL>2.0.CO;2](https://doi.org/10.1175/1520-0485(1973)003<0429:WIBMIL>2.0.CO;2)
- 733 Csanady, G. T. (1977). On the cyclonic mean circulation of large lakes. *Proceedings of the
 734 National Academy of Sciences U.S.A.*, 74(6), 2204–2208.
 735 <https://doi.org/10.1073/pnas.74.6.2204>
- 736 Endoh, S., Watanabe, M., Nagata, H., Maruo, F., Kawae, T., Iguchi, C., & Okumura, Y. (1995).
 737 Wind fields over Lake Biwa and their effect on water circulation. *Japanese Journal of
 738 Limnology (Rikusuigaku Zasshi)*, 56(4), 269–278. <https://doi.org/10.3739/rikusui.56.269>

- 739 Flood, B., Wells, M., Dunlop, E., & Young, J. (2020). Internal waves pump waters in and out of
 740 a deep coastal embayment of a large lake. *Limnology and Oceanography*, *65*(2), 205–
 741 223. <https://doi.org/10.1002/lno.11292>
- 742 Foroughan, M., Hamze-Ziabari, S.M., Lemmin, U., & Barry, D.A. (2022). A persistent
 743 submesoscale frontal slick: A novel marker of the mesoscale flow field in a large lake
 744 (Lake Geneva). *Geophysical Research Letters*. *49*(20), e2022GL100262.
 745 <https://doi.org/10.1029/2022GL100262>
- 746 Gaillard, R., Perroud, M., Goyette, S., & Kasparian, J. (2022). Multi-column modelling of Lake
 747 Geneva for climate applications. *Scientific Reports*, *12*(1), 353.
 748 <https://doi.org/10.1038/s41598-021-04061-6>
- 749 Gill, A. (1982). *Atmosphere-ocean dynamics*. *International Geophysics*, *30*, 612 pages. Elsevier.
- 750 Gula, J., Molemaker, M. J., & McWilliams, J. C. (2014). Submesoscale cold filaments in the
 751 Gulf Stream. *Journal of Physical Oceanography*, *44*(10), 2617–2643.
 752 <https://doi.org/10.1175/JPO-D-14-0029.1>
- 753 Gutiérrez, D., Bouloubassi, I., Sifeddine, A., Purca, S., Goubanova, K., Graco, M., et al. (2011).
 754 Coastal cooling and increased productivity in the main upwelling zone off Peru since the
 755 mid-twentieth century. *Geophysical Research Letters*, *38*(7), L07603.
 756 <https://doi.org/10.1029/2010GL046324>
- 757 Hamze-Ziabari, S. M., Lemmin, U., Soullignac, F., Foroughan, M., & Barry, D. A. (2022a).
 758 Basin-scale gyres and mesoscale eddies in large lakes: A novel procedure for their
 759 detection and characterization, assessed in Lake Geneva. *Geoscientific Model*
 760 *Development*, *15*, 8785–8807, <https://doi.org/10.5194/gmd-15-8785-2022>, 2022.
- 761 Hamze-Ziabari, S. M., Razmi, A. M., Lemmin, U., & Barry, D. A. (2022b). Detecting
 762 submesoscale cold filaments in a basin-scale gyre in large, deep Lake Geneva
 763 (Switzerland/France). *Geophysical Research Letters*, *49*(4), e2021GL096185.
 764 <https://doi.org/10.1029/2021GL096185>
- 765 Hui, Y., Farnham, D. J., Atkinson, J. F., Zhu, Z., & Feng, Y. (2021). Circulation in Lake Ontario:
 766 numerical and physical model analysis. *Journal of Hydraulic Engineering*, *147*(8),
 767 05021004. [https://doi.org/10.1061/\(ASCE\)HY.1943-7900.0001908](https://doi.org/10.1061/(ASCE)HY.1943-7900.0001908)
- 768 Hüsler, F., Fontana, F., Neuhaus, C., Riffler, M., Musial, J., & Wunderle, S. (2011). AVHRR
 769 archive and processing facility at the University of Bern: A comprehensive 1-km satellite
 770 data set for climate change studies. *EARSeL EProceedings*, *10*(2), 83–101.
- 771 Ishikawa, K., Kumagai, M., Vincent, W. F., Tsujimura, S., & Nakahara, H. (2002). Transport
 772 and accumulation of bloom-forming cyanobacteria in a large, mid-latitude lake: the gyre-
 773 microcystis hypothesis. *Limnology*, *3*(2), 87–96. <https://doi.org/10.1007/s102010200010>
- 774 Jane, S. F., Hansen, G. J. A., Kraemer, B. M., Leavitt, P. R., Mincer, J. L., North, R. L., et al.
 775 (2021). Widespread deoxygenation of temperate lakes. *Nature*, *594*(7861), 66–70.
 776 <https://doi.org/10.1038/s41586-021-03550-y>
- 777 Ji, Z.-G., & Jin, K.-R. (2006). Gyres and seiches in a large and shallow lake. *Journal of Great*
 778 *Lakes Research*, *32*(4), 764–775. [https://doi.org/10.3394/0380-1330\(2006\)32\[764:GASIAL\]2.0.CO;2](https://doi.org/10.3394/0380-1330(2006)32[764:GASIAL]2.0.CO;2)
- 780 Large, G., & Yeager, S. (2004). Diurnal to decadal global forcing for ocean and sea-ice models:
 781 The data sets and flux climatologies. <https://doi.org/10.5065/D6KK98Q6>
- 782 Laval, B. E., Imberger, J., & Findikakis, A. N. (2005). Dynamics of a large tropical lake: Lake
 783 Maracaibo. *Aquatic Sciences*, *67*(3), 337–349. [https://doi.org/10.1007/s00027-005-0778-](https://doi.org/10.1007/s00027-005-0778-1)
 784 1

- 785 Lemmin, U. (2016). Mouvements des masses d'eau (Water mass movement), In U. Lemmin
 786 (Ed.), *Dans les abysses du Léman* (Descent into the abyss of Lake Geneva), Presses
 787 Polytechniques et Universitaires Romandes (PPUR), Lausanne, Switzerland. ISBN: 978-
 788 2-88915-105-9.
- 789 Lemmin, U. (2020). Insights into the dynamics of the deep hypolimnion of Lake Geneva as
 790 revealed by long-term temperature, oxygen, and current measurements. *Limnology and*
 791 *Oceanography*, 65(9), 2092–2107. <https://doi.org/10.1002/lno.11441>
- 792 Lemmin, U., & D'Adamo, N. (1996). Summertime winds and direct cyclonic circulation:
 793 Observations from Lake Geneva. *Annales Geophysicae*, 14(11), 1207–1220.
 794 <https://doi.org/10.1007/s00585-996-1207-z>
- 795 Lovecchio, E., Gruber, N., Münnich, M., & Frenger, I. (2022). On the processes sustaining
 796 biological production in the offshore propagating eddies of the Northern Canary
 797 upwelling system. *Journal of Geophysical Research: Oceans*, 127(2), e2021JC017691.
 798 <https://doi.org/10.1029/2021JC017691>
- 799 Lu, Z., Wang, G., & Shang, X. (2020). Strength and spatial structure of the perturbation induced
 800 by a tropical cyclone to the underlying eddies. *Journal of Geophysical Research: Oceans*,
 801 125(5), e2020JC016097. <https://doi.org/10.1029/2020JC016097>
- 802 Lv, M., Wang, F., Li, Y., Zhang, Z., & Zhu, Y. (2022). Structure of sea surface temperature
 803 anomaly induced by mesoscale eddies in the North Pacific Ocean. *Journal of*
 804 *Geophysical Research: Oceans*, 127(3), e2021JC017581.
 805 <https://doi.org/10.1029/2021JC017581>
- 806 Marshall, J., Adcroft, A., Hill, C., Perelman, L., & Heisey, C. (1997). A finite-volume,
 807 incompressible Navier Stokes model for studies of the ocean on parallel computers.
 808 *Journal of Geophysical Research: Oceans*, 102(C3), 5753–5766.
 809 <https://doi.org/10.1029/96JC02775>
- 810 McWilliams, J. C. (2019). A survey of submesoscale currents. *Geoscience Letters*, 6(1), 3.
 811 <https://doi.org/10.1186/s40562-019-0133-3>
- 812 Mortimer, C. H. (2004). *Lake Michigan in motion: responses of an inland sea to weather, Earth-*
 813 *spin, and Human Activities*. Univ of Wisconsin Press.
- 814 Ostrovsky, I., & Sukenik, A. (2008). Spatial heterogeneity of biogeochemical parameters in a
 815 subtropical lake. In P. K. Mohanty (Ed.), *Monitoring and Modelling Lakes and Coastal*
 816 *Environments* (pp. 79–90). Dordrecht: Springer Netherlands. [https://doi.org/10.1007/978-](https://doi.org/10.1007/978-1-4020-6646-7_6)
 817 [1-4020-6646-7_6](https://doi.org/10.1007/978-1-4020-6646-7_6)
- 818 Pickett, M. H., & Paduan, J. D. (2003). Ekman transport and pumping in the California Current
 819 based on the U.S. Navy's high-resolution atmospheric model (COAMPS). *Journal of*
 820 *Geophysical Research: Oceans*, 108(C10), 3327. <https://doi.org/10.1029/2003JC001902>
- 821 Pisoni, J. P., Rivas, A. L., & Piola, A. R. (2014). Satellite remote sensing reveals coastal
 822 upwelling events in the San Matías Gulf—Northern Patagonia. *Remote Sensing of*
 823 *Environment*, 152, 270–278. <https://doi.org/10.1016/j.rse.2014.06.019>
- 824 Plattner, S., Mason, D. M., Leshkevich, G. A., Schwab, D. J., & Rutherford, E. S. (2006).
 825 Classifying and forecasting coastal upwellings in Lake Michigan using satellite derived
 826 temperature images and buoy data. *Journal of Great Lakes Research*, 32(1), 63–76.
 827 [https://doi.org/10.3394/0380-1330\(2006\)32\[63:CAFUI\]2.0.CO;2](https://doi.org/10.3394/0380-1330(2006)32[63:CAFUI]2.0.CO;2)
- 828 Pöschke, F., Lewandowski, J., Engelhardt, C., Preuß, K., Oczipka, M., Ruhtz, T., & Kirillin, G.
 829 (2015). Upwelling of deep water during thermal stratification onset—A major

- 830 mechanism of vertical transport in small temperate lakes in spring? *Water Resources*
831 *Research*, 51(12), 9612–9627. <https://doi.org/10.1002/2015WR017579>
- 832 Rahaghi, A. I., Lemmin, U., Cimatoribus, A. A., & Barry, D. A. (2019). The importance of
833 systematic spatial variability in the surface heat flux of a large lake: A multiannual
834 analysis for Lake Geneva. *Water Resources Research*, 55(12), 10248–10 267.
835 <https://doi.org/10.1029/2019WR024954>
- 836 Rahaghi, A.I., Lemmin, U., Cimatoribus A., Bouffard, D., Riffler, M., Wunderle, S., & Barry,
837 D.A. (2018). Improving surface heat flux estimation for a large lake through model
838 optimization and two-point calibration: The case of Lake Geneva. *Limnology and*
839 *Oceanography: Methods*, 16(9), 576–593. <https://doi.org/10.1002/lom3.10267>
- 840 Reiss, R. S., Lemmin, U., Cimatoribus, A. A., & Barry, D. A. (2020). Wintertime coastal
841 upwelling in Lake Geneva: An efficient transport process for deepwater renewal in a
842 large, deep lake. *Journal of Geophysical Research: Oceans*, 125(8), e2020JC016095.
843 <https://doi.org/10.1029/2020JC016095>
- 844 Reiss, R. S., Lemmin, U., & Barry, D. A. (2022). Wind-induced hypolimnetic upwelling between
845 the multi-depth basins of Lake Geneva during winter: An overlooked deepwater renewal
846 mechanism? *Journal of Geophysical Research: Oceans*, 127(6), e2021JC018023.
847 <https://doi.org/10.1029/2021JC018023>
- 848 Riffler, M., Lieberherr, G., & Wunderle, S. (2015). Lake surface water temperatures of European
849 Alpine lakes (1989–2013) based on the Advanced Very High Resolution Radiometer
850 (AVHRR) 1 km data set. *Earth System Science Data*, 7(1), 1–17.
851 <https://doi.org/10.5194/essd-7-1-2015>
- 852 Romanovsky, V. V., & Shabunin, G. D. (2002). Currents and vertical water exchange in Lake
853 Issyk Kul. In J. Klerkx & B. Imanackunov (Eds.), *Lake Issyk-Kul: Its Natural*
854 *Environment* (pp. 77–87). Dordrecht: Springer Netherlands. [https://doi.org/10.1007/978-](https://doi.org/10.1007/978-94-010-0491-6_7)
855 [94-010-0491-6_7](https://doi.org/10.1007/978-94-010-0491-6_7)
- 856 Rowe, M. D., Anderson, E. J., Beletsky, D., Stow, C. A., Moegling, S. D., Chaffin, J. D., et al.
857 (2019). Coastal upwelling influences hypoxia spatial patterns and nearshore dynamics in
858 Lake Erie. *Journal of Geophysical Research: Oceans*, 124(8), 6154–6175.
859 <https://doi.org/10.1029/2019JC015192>
- 860 Schwab, D. J., & Beletsky, D. (2003). Relative effects of wind stress curl, topography, and
861 stratification on large-scale circulation in Lake Michigan. *Journal of Geophysical*
862 *Research: Oceans*, 108(C2), 3044. <https://doi.org/10.1029/2001JC001066>
- 863 Schwab, D. J., O'Connor, W. P., & Mellor, G. L. (1995). On the net cyclonic circulation in large
864 stratified lakes. *Journal of Physical Oceanography*, 25(6), 1516–1520.
865 [https://doi.org/10.1175/1520-0485\(1995\)025<1516:OTNCCI>2.0.CO;2](https://doi.org/10.1175/1520-0485(1995)025<1516:OTNCCI>2.0.CO;2)
- 866 Shimizu, K., Imberger, J., & Kumagai, M. (2007). Horizontal structure and excitation of primary
867 motions in a strongly stratified lake. *Limnology and Oceanography*, 52(6), 2641–2655.
868 <https://doi.org/10.4319/lo.2007.52.6.2641>
- 869 Strub, P. T., & Powell, T. M. (1986). Wind-driven surface transport in stratified closed basins:
870 Direct versus residual circulations. *Journal of Geophysical Research: Oceans*, 91(C7),
871 8497–8508. <https://doi.org/10.1029/JC091iC07p08497>
- 872 Troitskaya, E., Blinov, V., Ivanov, V., Zhdanov, A., Gnatovsky, R., Sutyryna, E., & Shimaraev,
873 M. (2015). Cyclonic circulation and upwelling in Lake Baikal. *Aquatic Sciences*, 77(2),
874 171–182. <https://doi.org/10.1007/s00027-014-0361-8>

- 875 Valbuena, S. A., Bombardelli, F. A., Cortés, A., Largier, J. L., Roberts, D. C., Forrest, A. L., &
876 Schladow, S. G. (2022). 3D flow structures during upwelling events in lakes of moderate
877 size. *Water Resources Research*, *58*(3), e2021WR030666.
878 <https://doi.org/10.1029/2021WR030666>
- 879 Valerio, G., Cantelli, A., Monti, P., & Leuzzi, G. (2017). A modeling approach to identify the
880 effective forcing exerted by wind on a prealpine lake surrounded by a complex
881 topography. *Water Resources Research*, *53*(5), 4036–4052.
882 <https://doi.org/10.1002/2016WR020335>
- 883 Vallis, G. K. (2017). *Atmospheric and oceanic fluid dynamics: fundamentals and large-scale*
884 *circulation* (2nd ed.). Cambridge: Cambridge University Press.
885 <https://doi.org/10.1017/9781107588417>
- 886 Voudouri, A., Avgoustoglou, E., & Kaufmann, P. (2017). Impacts of observational data
887 assimilation on operational forecasts. In T. Karacostas, A. Bais, & P. T. Nastos (Eds.),
888 *Perspectives on Atmospheric Sciences* (pp. 143–149). Cham: Springer International
889 Publishing. https://doi.org/10.1007/978-3-319-35095-0_21
- 890 Wang, B., & An, S.-I. (2005). A method for detecting season-dependent modes of climate
891 variability: S-EOF analysis. *Geophysical Research Letters*, *32*(15), L15710.
892 <https://doi.org/10.1029/2005GL022709>
- 893 Xu, W., Collingsworth, P. D., & Minsker, B. (2019). Algorithmic characterization of lake
894 stratification and deep chlorophyll layers from depth profiling water quality data. *Water*
895 *Resources Research*, *55*(5), 3815–3834. <https://doi.org/10.1029/2018WR023975>
- 896 Zhang, Z., Qiu, B., Klein, P., & Travis, S. (2019). The influence of geostrophic strain on oceanic
897 ageostrophic motion and surface chlorophyll. *Nature Communications*, *10*(1), 2838.
898 <https://doi.org/10.1038/s41467-019-10883-w>
899